Rigid and Flexible Foils Oscillating Near a Free Surface

D.J. Cleaver[*], D.E. Calderon[†], Z. Wang[‡], and I. Gursul[§]
University of Bath, Bath, BA2 7AY, United Kingdom

Experiments were performed for rigid and flexible foils oscillating near a free surface. The results presented investigate the effect of amplitude, depth and flexible trailing-edge devices on the drag reduction of a NACA 0012 airfoil plunging at a range of frequencies. At low Strouhal number based on amplitude, Sr_A, the drag reduction follows a parabolic trend with greater effect for greater amplitude, similar to Garrick predictions. At $Sr_A \approx 0.08$ larger amplitudes break from this trend due to leading-edge vortex formation. As a result smaller amplitudes become preferable for $Sr_A > 0.12$. The effect of depth is twofold, firstly with decreasing depth there is a general departure from Garrick trends. Secondly a reduction in thrust is observed around a constant unsteady parameter of $\tau \approx 0.25$; around this value significant free surface waves form that detract from thrust creation. For depths greater than two chords there is negligible free surface effect. Flexible trailing edge devices are shown to increase drag reduction by up to 28%. The device acts to strengthen the trailing-edge vortices leading to a stronger time-averaged jet. They are more effective with larger device length and at smaller amplitudes, but still improve drag reduction for all amplitudes across a wide range of rigidities. The optimal elastic parameter is shown to be on the order of unity.

Nomenclature

a	=	amplitude of plunging motion
A	=	peak to peak amplitude of plunging motion
C_d	=	time-averaged drag coefficient
C_{d0}	=	time-averaged drag coefficient for the stationary airfoil
c	=	chord length
d	=	depth
E	=	Young's modulus
f	=	frequency
Fr	=	Froude number, $U_\infty/\sqrt{(gc)}$
I	=	second moment of area
L_{TED}	=	trailing-edge device length
Re	=	Reynolds number, $\rho U_\infty c/\mu$
Sr_c	=	Strouhal number based on chord, fc/U_∞
Sr_A	=	Strouhal number based on amplitude, $2fa/U_\infty$
s	=	trailing-edge device thickness
t	=	time, t = 0 is top of motion
T	=	plunge period
U_{PL}	=	peak plunge velocity, $2\pi fa$
U_∞	=	free stream velocity
x_{TE}	=	streamwise position of trailing-edge
x_{TIP}	=	streamwise position of trailing-edge device tip
y_{TE}	=	cross-stream position of trailing-edge

[*] Research Officer, Department of Mechanical Engineering, Member AIAA.
[†] Postgraduate Student, Department of Mechanical Engineering, Student Member AIAA.
[‡] Lecturer, Department of Mechanical Engineering, Member AIAA.
[§] Professor, Department of Mechanical Engineering, Associate Fellow AIAA.

y_{TIP} = cross-stream position of trailing-edge device tip
α = angle of attack
Γ = circulation
δ = flap angle amplitude
λ = elastic parameter, $(Es^3/12)/(0.5\rho(U_\infty^2+U_{pl}^2)L_{TED}^3)$
λ_w = wavelength of water wave
μ = viscosity
ρ = density
τ = unsteady parameter, $U_\infty 2\pi f/g$
φ_δ = flap phase lead

I. Introduction

There is currently the demand for naval vessels to go faster, more efficiently. To achieve this it will be necessary to use some form of drag reduction. Promising technologies based on injection of microbubbles [1,2] and polymers [3] into the boundary layer have been developed in laboratory tests for stationary surfaces and foils. Although these technologies have demonstrated great potential for drag reduction (as much as 80%) at low speeds and for stationary surfaces, they are not proven for realistic conditions where the vessel motion is at high speed and unsteady. As an alternative drag reduction method, we propose the application of passively produced plunging motion for high speed hydrofoil vessels. Within the field of unsteady aerodynamics it is well established [4-8] that the drag coefficient of a plunging foil is significantly less than that of a steady foil even to the extent that it is possible for the plunging foil to create thrust. Furthermore the technique is well established in nature, and has previously been applied [9] to low speed vessels to extract wave energy and improve stability.

Foil oscillations reduce drag through the Knoller-Betz effect. A stationary foil will shed vortices in the classic Kármán vortex street pattern. This is taken to be drag indicative due to the momentum deficit in the wake. As the airfoil is oscillated with increasing frequency or amplitude the positions of these vortices will be gradually inverted to create a reverse-Kármán vortex street. This is taken to be thrust indicative due to the momentum surplus in the wake. The most influential parameter in determining the thrust performance of the motion is generally accepted as the nondimensional plunge velocity, $Sr_A = fA/U_\infty$. It is therefore effective for both high-frequency small-amplitude motion, and low-frequency large-amplitude motion.

For a high speed hydrofoil vessel there are two possible methods of creating the motion, either actively through forced motion (Fig. 1a) or passively through wave motion (Fig. 1b). The active scenario will give the greatest control but will also require work input. The passive scenario is the more interesting possibility as it requires no work input and indeed any hydrofoil passing through waves will experience the effect regardless of whether it is intended. In essence as the craft passes through the waves it will be subject to an oscillatory freestream due to both the oscillatory flow within the waves and also the motion of the vessel reacting to the waves. The maximum feasible amplitude of this motion is therefore the amplitude of the wave, and the frequency of the motion can be estimated through the wave encounter frequency, $f \approx U_\infty/\lambda_w$. Using these definitions a selection of realistic wave amplitudes and frequencies from the Pierson-Moskowitz sea spectrum, are shown as symbols in Fig. 2 for two possible hydrofoil chord lengths. Conveniently this real wave data approximately collapses onto a constant Strouhal number based on amplitude of $Sr_A = 0.076$ which is independent of vessel speed, hydrofoil chord length and sea state. Although this real wave data represents a realistic operating scenario it is solely for the significant wave as derived from a wave spectra, and therefore does not give a maximum Sr_A. Thus to give an absolute upper bound, also shown is the value for a Stokes ideal wave of $A/\lambda_w = 1/7$, or alternately $Sr_A = 0.142$ [10,11]. This is a theoretical value for an ideal wave of maximum steepness which realistically will not be surpassed and therefore represents an excellent upper bound for the experiments.

In addition it has previously been demonstrated [12] that this drag reduction can be further enhanced through the correct application of flexibility. It was shown that that for a foil with a $c/3$ teardrop section and $2c/3$ flexible flat plate the correct application of flexibility could increase drag reduction by up to 100%. Flexibility acted to enhance trailing-edge vortex strength and spacing so as to increase the momentum surplus in the reverse-Kármán vortex street. It was also demonstrated that the motion could be considered as analogous to a heaving-pitching foil. The heaving motion is actively produced and the pitching motion is passively produced through deformation of the

flexible part. Indeed the optimal phase lag between pitch and heave was 95° to 100° consistent with studies for rigid foils undergoing combined heave and pitch.

To investigate the possibility of drag reduction through small-amplitude airfoil oscillation, the first part of this paper shall examine the effect of amplitude and depth for a NACA 0012 airfoil oscillating horizontally near a free surface at plunge velocities up to $Sr_A = 0.16$. The motion is sinusoidal as this is the best approximation possible to the two scenarios shown in Fig. 1. The second part shall examine if this drag reduction can be enhanced through the use of small ($\leq 0.3c$) flexible trailing-edge devices.

II. Experimental Apparatus and Procedures

Force and Particle Image Velocimetry (PIV) measurements were conducted on a plunging NACA 0012 airfoil mounted horizontally in a closed-loop water tunnel, see Fig. 3. For a review of parameters studied, see Table 1; uncertainties are calculated based on the methods of Moffat [13] taking into account both bias and precision errors.

Table 1 Experimental Parameters

Parameter	Range Considered	Uncertainty
Re	40,000	+/- 200
α	0°	+/- 0.5°
a/c	0.1 to 0.5	+/- 0.003
Sr_c	0 to 0.8	+/- 2.3%
Sr_A	0 to 0.16	+/- 0.0012
d/c	0.5 to 2.25	+/- 0.02
Fr	0.43	+/- 0.03

A. Experimental Setup

The experiments were conducted in a free-surface closed-loop water tunnel (Eidetics Model 1520) at the University of Bath. The water tunnel is capable of flow speeds in the range 0 to 0.5 m/s and has a working section of dimensions 381 mm x 508 mm x 1530 mm. The turbulence intensity has previously [14] been measured by LDV to be less than 0.5%.

Mounted on top of the tunnel is the experimental rig, see Fig. 3b. This consists of a carriage mounted on New Way air bushings, which is driven by an Aerotech BLMC linear motor controlled by an Aerotech Soloist CP controller with position feedback from a Renishaw Signum optical encoder. This system was capable of achieving sinusoidal oscillations of arbitrary amplitude and depth with a maximum recorded position error of < 30μm. Attached to this carriage is the binocular force balance described below. The wing is attached to the force balance through two, 2 mm thick, streamlined stainless steel stings mounted at either end. The wing spanned the test section wall to wall with a 2 mm clearance so as to minimise three-dimensional effects. Four cross sections are considered: a NACA 0012 airfoil, and three NACA 0012 airfoils with flexible trailing-edge device of differing lengths, see Fig. 4. The total chord length of all cross sections was maintained at 100 mm. For the three flexible trailing-edge device wings this meant adjusting the NACA chord length to maintain 1.4 mm thickness at 90 mm ($L_{TED} = 0.1c$), 80 mm ($L_{TED} = 0.2c$), or 70 mm ($L_{TED} = 0.3c$) from the leading-edge. The thickness therefore varies between wings. All wings were constructed by selective laser sintering from glass filled polyamide.

For the flexible trailing-edge device to practically achieve an acceptable range of rigidity four different materials in a wide range of thicknesses were used:

- 6 x stainless steel - $E = 205$ x 109 Nm^{-2}, $s = 0.025$ mm to 1 mm.
- 1 x aluminium - $E = 69$ x 109 Nm^{-2}, $s = 0.025$ mm.
- 7 x polyester - $E = 3.5$ x 109 Nm^{-2}, $s = 0.013$ mm to 0.127 mm.
- 7 x vinyl - $E = 3.4$ x 109 Nm^{-2}, $s = 0.191$ mm to 0.762 mm.

This gives a choice of 21 possible rigidities (EI) over a very wide spread, see Fig. 4. The trailing-edge devices were secured in the 1mm groove at the rear of the airfoil using grub screws embedded in tapped inserts. These were filled, smoothed, and repainted each time.

B. Force Measurements

The force in the streamwise direction was measured through a two-component binocular strain gauge force balance [15]. Two force balances of differing rigidities were used so as to achieve the desired accuracy whilst minimizing flexibility. The signal from the strain gauges was amplified by a Wheatstone bridge circuit and sampled at either 2 kHz for 21,600 samples (stationary cases), or 360 per cycle for a minimum of 60 cycles (dynamic cases). The forces were then calculated from the average voltage through linear calibration curves. The calibration curves consisted of thirteen points, and were performed daily before testing. Each data set was repeated at least once and then averaged.

To validate the accuracy of the method, force measurements were performed for a/c = 0.1 and 0.2 and compared to those taken using the vertical rig described in Heathcote et al. [16], Calderon et al. [17], and Cleaver et al. [4,8,18,19] with the same experimental conditions. This vertical rig is an entirely different setup which mounts the airfoil vertically between two end plates and therefore does not experience free surface effects. Despite the significant differences the agreement between the two is excellent, see Fig. 5.

C. PIV Measurements

The flow was seeded with 8 – 12 μm hollow glass spheres. The velocity field around the airfoil was measured using a TSI Inc. 2D-PIV system incorporating a dual ND:YAG 50 mJ pulsed laser, 2 MP Powerview Plus 12 bit CCD camera and TSI Model 610034 synchronizer. For the majority of the measurements the laser was positioned behind to illuminate a mid-span streamwise plane with the camera positioned to the side as shown in Fig. 3a. For the measurements over the leading-edge region at d/c = 0.5 it was necessary to reposition the laser above the free surface, aimed downwards, so as to capture the free surface and the leading-edge region. The PIV images were analyzed using the software Insight 3G. A FFT correlator using interrogation windows of 32 x 32 pixels with 50% overlap was selected to generate a vector field of 99 x 73 vectors, approximately giving a 2.5 mm spatial resolution. The phase-averaged data is derived from 100 pairs of images; the time-averaged data is derived from 500 pairs of images. Measurements over the aft region and leading-edge region were performed separately. Where necessary these were then merged in MATLAB through interpolation of the aft region data onto the leading-edge region grid using the trailing-edge as the common reference point.

D. Deformation Measurements

For each case detailed instantaneous and phase-locked PIV measurements were performed across a range of Strouhal numbers. Since the deformation of the trailing-edge device is predominantly two-dimensional, i.e., the same across the span, it was possible to also derive the deformation of the trailing-edge device from the laser sheet slice in the PIV images. The flap angle was derived from the position of the tip of the trailing-edge device and the trailing-edge of the airfoil, see Fig. 6a. In MATLAB a sine fit was then applied to define the amplitude and phase lead of the deformation. A typical example is shown in Fig. 6b, generally the fit was excellent.

III. Results and Discussion

A. Effect of Amplitude

Shown in Fig. 7 is the drag reduction for a NACA 0012 airfoil oscillated at the central depth, d/c = 2.25, for a range of amplitudes against non-dimensional frequency in the form of Sr_c. For all cases increasing amplitude or frequency leads to increased drag reduction. For the smaller amplitudes (a/c = 0.1 and 0.2) this trend is strongly parabolic with steeper gradient for greater amplitude. For the larger amplitudes (a/c = 0.3, 0.4 and 0.5) there is still a parabolic trend with steeper gradient for greater amplitude at lower Strouhal numbers, but at higher Strouhal numbers there is a 'kink' which causes a break from this trend. We shall return to this later. The strong amplitude dependence is expected since Garrick approximations predict the thrust (drag reduction) from an oscillating airfoil to be:

$$C_T = \pi^3 Sr_A^2 (F^2 + G^2)$$

Where F and G are the Theodorsen functions which are weakly dependent on the frequency, Sr_c, and the far more influential parameter, Sr_A, is dependent on both amplitude and frequency. Sr_A can be considered as a non-dimensional plunge velocity. Since Sr_A is the more influential parameter, and as it is more applicable to our problem (see Fig. 2), any further results shall be presented against Strouhal number based on amplitude.

Fig. 8 shows the same results as Fig. 7 except with Strouhal number based on amplitude on the x-axis. The collapse in the data reiterates the importance of Strouhal number based on amplitude. Also shown are dashed lines which represent the Garrick approximations for the same five amplitudes. These demonstrate parabolic trends with steeper

gradient for greater amplitude. At low Strouhal number ($Sr_A < 0.08$) the experimental results follow these general trends but with reduced gradients in comparison with the Garrick approximations. The reason for the difference can be attributed to the limitations of Garrick approximations. In particular Garrick approximations are inviscid, assume no separation and apply in the limit of small-amplitude motion. As demonstrated by other authors [6,12] Garrick approximations therefore tend to over predict thrust generation. At $Sr_A \approx 0.08$ the aforementioned kink means that the larger amplitudes break from this general trend resulting in a crossover point at $Sr_A \approx 0.12$. Thus for the same plunge velocity before $Sr_A \approx 0.12$ larger a/c is preferable; after $Sr_A \approx 0.12$ smaller a/c becomes preferable. The collapse of data at this particular point is most likely coincidental, indeed the curve for $a/c = 0.2$ does not crossover the $a/c = 0.1$ curve until $Sr_A \approx 0.14$.

To investigate why larger amplitudes break from the parabolic Garrick trend phase-averaged PIV measurements were performed for $Sr_A = 0.04$, 0.08, 0.12, and 0.16 for the smallest and largest amplitudes, see Fig. 9 through 12. Fig. 9 shows $Sr_A = 0.04$ at the top, middle (down), bottom, and middle (up) phases of the motion. For both amplitudes at this low Strouhal number Kelvin-Helmholtz instability dominates, generating a series of small alternating vortices which are shed at high frequency from the trailing-edge. It is interesting that these instabilities should appear in phase-averaged measurements because for the vortices not to be eradicated through the averaging process they must be locked in to the phase of the motion. Young and Lai [20] performed a computational study on a NACA 0012 airfoil at $\alpha = 0°$ and $Re = 20{,}000$ which predicted that the airfoil would be subject to vortex lock-in in a similar manner to oscillating cylinders. This means that at low Strouhal numbers the natural shedding frequency dominates, at high Strouhal numbers the forcing frequency dominates, and in between there may be a harmonic region. The harmonic region means that the airfoil may display vortex shedding at a higher harmonic of the forcing frequency. Taking into account the slightly higher natural shedding frequency [21] at this higher Reynolds number and using the lock-in boundaries presented in Young and Lai [20], the frequency-amplitude combinations shown in Figs. 9 through 12 should be firmly within the harmonic region. Hence the shedding is not random but a harmonic of the plunging frequency resultant from the interplay between natural shedding and forcing frequency, and the vortices are therefore locked-in to the phase of the motion and visible in a phase-averaged sense.

$Sr_A = 0.08$ (Fig. 10) is the point at which $a/c = 0.5$ breaks from the Garrick trend. The vortices are now stronger and the forcing frequency is becoming more dominant. This is more clearly exhibited for $a/c = 0.1$ where multiple vortices are being shed per half cycle but they are being shed in groups locked into the phase of the motion. Hence during the downward motion multiple counter-clockwise vortices emanating from the lower surface shear layer are shed, and during the upward motion multiple clockwise vortices emanating from the upper surface shear layer are shed. For the larger amplitude the low Sr_c means that this is less evident because the natural shedding frequency is still dominant.

$Sr_A = 0.12$ (Fig. 11) is after the $a/c = 0.5$ drag reduction curve breaks from the theoretical Garrick trend. There is now significantly different behavior for $a/c = 0.5$. At the top of the motion there is a large counter-clockwise leading-edge vortex below the trailing-edge; likewise at the bottom of the motion there is a large clockwise leading-edge vortex above the trailing-edge. These convected LEVs are unstable and lose their coherency more rapidly as evidenced by their rapid dissipation in a phase-averaged sense. Similar unstable LEVs have been shown to exist at lower Reynolds numbers for smaller amplitudes and higher frequencies [8] and the instability has been shown to be promoted by higher Reynolds numbers [22]. In these cases, spanwise instabilities resulted in their abrupt breakdown and complete dissipation. In the current measurements the convected LEV is weak but still existent. Its circulation is therefore reduced and as predicted by von Kármán and Burgess's equation for thrust due to a reverse-Kármán vortex street [23], the thrust generated will also be reduced. Similar deteriorating thrust performance due to leading-edge separation has previously been observed by Tuncer and Kaya [24] for a plunging NACA 0012 airfoil. The onset of separation was found to be $Sr_A \approx 0.11$, however this became a poor approximation at smaller amplitudes ($a/c < 0.3$) where larger plunge velocities are required. In addition Garrick approximations assume no separation, consequently the presence of these leading-edge vortices is a strong explanation for the break from Garrick trends. The question is therefore why are smaller amplitudes less prone to separation and LEVs despite having the same maximum plunge velocity and therefore the same peak effective angle of attack? The core reason for this difference is that to achieve the same Sr_A at larger amplitude requires lower frequency, thus there is a larger formation and convection time per cycle. It is therefore necessary to also consider Sr_c, as this represents a ratio of the convection time scale (c/U_∞) to the motion time scale (f).

Sr_A = 0.16 (Fig. 12) is now after the crossover point. For a/c = 0.1 the vortices are now much stronger and the forcing frequency is clearly dominant although there are still multiple TEVs shed per half cycle suggesting that it is still within the harmonic region. These TEVs form a clear reverse-Kármán vortex street. There is a small LEV very close to the lower surface of the airfoil at the top of motion which convects along the lower surface gradually dissipating. For a/c = 0.5 the convected LEVs are now much stronger and dominate the flow field, see top and bottom of the motion.

In summary, the difference between the two amplitudes is that a/c = 0.1 is characterized by shedding of vorticity from the trailing-edge leading to a clear reverse-Kármán vortex street at higher Sr_A, whereas a/c = 0.5 is characterized by shedding from the leading-edge and therefore a weaker reverse-Kármán vortex street and diminished thrust performance.

B. Effect of Depth

Shown in Fig. 13 are drag reduction measurements for a further four depths: d/c = 2.00, 1.50, 1.00 and 0.50, and all five amplitudes. As one would expect d/c = 2.00 (Fig. 13a) is so close to the central depth (d/c = 2.25, Fig. 8) that the curves are essentially the same for all amplitudes. The only noticeable difference is perhaps the presence of a very weak peak at Sr_A = 0.09 for a/c = 0.2 (note the change in gradient); however this is contained within the bounds of experimental uncertainty and therefore cannot be confirmed as real.

At d/c = 1.50 (Fig. 13b) the peak at Sr_A = 0.09 for a/c = 0.2 is now clear and distinct. There is also further peaks for a/c = 0.3 at Sr_A = 0.13 and a/c = 0.4 at $Sr_A \approx 0.16$ although this last peak could actually be outside the measured range. Except for the existence of these peaks the general Garrick trends still hold true at low Strouhal numbers. At high Strouhal numbers the data has become more disordered and there is no longer a clear crossover point.

At d/c = 1.00 (Fig. 13c) the Garrick trends at low Strouhal number are now beginning to break down and there is a general departure from the trends observed for the central depth. Furthermore the peaks are now very distinct and occur at the same Strouhal numbers as for d/c = 1.50 with only minor deviation. In addition there is potentially a fourth weak peak for a/c = 0.1 at $Sr_A \approx 0.05$.

At d/c = 0.50 (Fig. 13d) the peak for a/c = 0.1 is now clear at Sr_A = 0.04 and the peaks for the other amplitudes are further accentuated. There is no longer any of the trends that were observed for the central depth. The effect of depth is therefore twofold: firstly with decreasing depth there is a gradual departure from the Garrick trends and crossover point observed for the central depth descending into more disorderly behavior; secondly drag enhancing peaks are observed at larger Strouhal numbers for larger amplitude. In addition it can also be concluded that the free surface has negligible effect at depths greater than two chords. This is in agreement with the earlier comparison shown in Fig. 5 and the computational results of Zhu et al. [25] for a horizontal NACA 0012 wing oscillating under a free surface.

Zhu et al. [25] also observed similar drag enhancing peaks. They attributed the cause to be oscillation at or around a critical unsteady parameter of $\tau_c = U_\infty 2\pi f/g$ = 0.25. At $\tau \approx 0.25$ the free surface wave field becomes dominated by the unsteady waves produced by the plunging motion rather than waves formed by the forward motion. Shown in Fig. 14 is therefore the same results plotted against the unsteady parameter, τ. The peaks collapse reasonably well around τ = 0.25 in support of this hypothesis.

To obtain further detail on the cause of the peaks, phase-averaged PIV measurements were performed for a/c = 0.2 and Sr_c = 0.150, 0.225, and 0.300, at both the central depth and the shallowest depth. The associated force measurements are shown in Fig. 15, and the PIV measurements are shown in Figures 16 through 18. The left column shows the shallowest depth, d/c = 0.5; the right column shows the central depth, d/c = 2.25. Both show phase-averaged velocity magnitude for the top, middle (down), bottom, and middle (up) phases of the motion. For d/c = 0.5 the free surface is demarked by a solid black line. The streamlines on some plots can be seen ending or starting on either the free surface or the airfoil. This is due to both the airfoil and free surface being in motion.

Sr_c = 0.150 (Fig. 16) is before the d/c = 0.50 peak. For this Strouhal number there is some minor wave formation, most prominently in the middle (down) phase (Fig. 16b). Despite this wave formation the flow fields are comparatively similar. There is a region of lower velocity over the leading-edge at the top of the motion (Fig. 16a), and a high velocity region over the aft of the airfoil in the middle (down, Fig. 16b) and bottom phases (Fig. 16c).

Given this combination one would expect the drag force coefficient to be slightly larger for the shallowest depth which is in agreement with the force measurements (Fig. 15).

Sr_c = 0.225 (Fig. 17) is at the d/c = 0.50 peak. As can be seen by the shape of the free surface, the wave formation is significantly larger for this Strouhal number. The effect of these waves on the flow field is significant. This is most pronounced at the shallowest point in the motion (Fig. 17a) where the entire airfoil is engulfed in a low velocity region in contrast to the central depth. In the next phase (Fig. 17b) there is a small LEV at the central depth which is absent for the shallowest depth. Furthermore the shape of the streamlines are significantly different, for d/c = 2.25 the streamlines curve around the LEV, whereas for d/c = 0.5 due to the motion of the free surface the streamlines emanate from the surface of the airfoil. At the bottom of the motion (Fig. 17c) although the streamlines are again similar for both depths, the aft of the airfoil at the shallowest depth is surrounded by a high velocity region. In the middle (up, Fig. 17d) phase this high velocity region persists although significantly weakened. At this phase the existence of significant waves is most apparent, and the effect of this wave is significant as demonstrated by the significantly different streamlines and velocity magnitude values.

Sr_c = 0.300 (Fig. 18) is after the d/c = 0.50 peak. For this Strouhal number although there is still wave formation it is significantly less, and therefore has a reduced effect on the flow field. At the top of the motion (Fig. 18a) the streamlines are similar across the two depths, although the flow is marginally decelerated by the proximity of the free surface at the shallowest depth. At the middle (down, Fig. 18b) phase of the motion a LEV is apparent for both depths, although the size and position is slightly different between the depths. The remnants of this LEV can also be seen at the central depth at the bottom of the motion (Fig. 18c). This is absent for the shallowest depth, instead the aft of the airfoil is surrounded by a high velocity region. At the next phase (Fig. 18d) the two depths are so similar as to be nearly identical.

In summary, for Sr_c = 0.150 and 0.300 the flow fields for the two depths, although subject to minor differences, are generally similar justifying the similar levels of drag reduction. For Sr_c = 0.225 the flow fields demonstrated significant wave formation at the shallowest depth. As a result the flow fields are significantly different justifying the difference in the level of drag reduction. It can therefore be concluded that the cause of the peaks is wave formation due to oscillation at or near an unsteady parameter value of τ = 0.25.

C. Effect of Flexibility

Shown in Fig. 19 is the reduction in drag coefficient for an airfoil with a flexible trailing-edge device of length L_{TED} = 0.2c for three amplitudes a/c = 0.1, 0.2 and 0.5, and a wide range of flexibilities. The results for a/c = 0.1 (Fig. 19a) demonstrate the same parabolic trend as observed for the NACA 0012 airfoil, however in this case the gradient is determined by the flexibility. Initially, decrease in rigidity from the rigid case (EI = 1.7 x 10^1 Nm, denoted by solid lines and circles), results in increasing gradient and therefore increasing drag reduction, leading to an optimum at EI = 2.1 x 10^{-3} Nm (denoted by solid lines and right triangles). Further decrease in rigidity beyond this optimum (denoted by dashed lines) results in decreasing performance.

At a/c = 0.2 (Fig. 19b) there are similar trends however the overall effect of flexibility is greatly diminished. Hence although there are trends similar to the NACA 0012 airfoil with the flexibility determining the gradient to give an optimum flexibility (EI = 6.0 x 10^{-4} Nm), the difference between this optimum and the rigid case is proportionally smaller. Likewise at a/c = 0.5 (Fig. 19c) the curves again follow the same trends observed for the NACA 0012 airfoil but the effect of flexibility is now so greatly diminished that it is not possible to define an optimum to within the bounds of experimental uncertainty.

Fig. 20 reiterates this amplitude dependence through the comparison of peak drag reduction, defined as the increase in drag reduction over the rigid case at the maximum Sr_A, against elastic parameter:

$$\lambda = \frac{\frac{Es^3}{12}}{0.5\rho(U_\infty^2 + U_{PL}^2)L_{TED}^3}$$

The elastic parameter can be considered as the nondimensional ratio of the rigidity, EI, to the driving force, the dynamic pressure. Fig. 20b is for the L_{TED} = 0.2c flexible trailing-edge device. It demonstrates that flexibility can be advantageous over a very wide range of flexibilities (note the log scale), with an optimum of $\lambda = O(1)$. In addition it is more effective for smaller amplitude resulting in a peak effectiveness of 24% for a/c = 0.1. Note that although this

curve is only for $Sr_A = 0.16$, due to the parabolic nature of the curves (see Fig. 19) it is reasonable to expect similar curves at lower Strouhal numbers. The largest Strouhal number was solely chosen so as to minimize the effect of experimental uncertainty.

Similar curves for $L_{TED} = 0.1c$ and $0.3c$ are shown in Fig. 20a and 20c respectively. The smaller trailing-edge device generates, although a generally still positive increase, a smaller increase in drag reduction. Smaller amplitude is again more effective and both amplitudes exhibit an optimum although this time in the region of $\lambda \approx 0.2$. The larger trailing-edge device creates larger increase in drag reduction, see Fig. 20c. It is again more effective at smaller amplitude leading to a peak improvement of 28% for $a/c = 0.1$. The optimum for this larger device is in the region of $\lambda \approx 3$.

To understand how flexibility improves drag reduction, three flexibilities for $L_{TED} = 0.2c$ and $a/c = 0.1$ were studied in detail through PIV and deformation measurements. These three cases are labeled rigid, optimal, and post-optimal in Fig. 20b. A typical example of the deformation measurements for an individual rigidity and Sr_A is shown in Fig. 21. The solid line is the motion of the trailing edge, and the dash-dot line the motion of the tip of the trailing edge device. The difference between the two is therefore the deformation of the trailing edge device (dashed line). Note that although the tip motion only slightly lags the trailing edge, the deformation has a significant phase lead.

Shown in Fig. 22 is the amplitude of this deformation in the form of flap angle (see Fig. 6a for definition), and its phase lead. As expected for the rigid case the flap angle amplitude is zero across all Strouhal numbers. For the optimal case the amplitude increases monotonically with Strouhal number leading to a maximum of $\delta = 8°$. For the post-optimal case the gradient is steeper resulting in a greater maximum of $\delta = 21°$. The phase lead of this deformation is shown in Fig. 22b. It was not possible to measure a phase lead for the rigid case because the deformation was negligible. With decreasing rigidity there is decreasing phase lead as previously observed by Heathcote et al. [12] for a larger trailing-edge device length.

The effect of deformation on the level of drag reduction is shown in Fig. 23. This demonstrates that optimal flexibility results in a steeper negative gradient and therefore greater reduction in drag coefficient for the same deformation. Hence it is not purely a matter of achieving the maximum level of deformation, but a combination of deformation and phasing through optimal flexibility.

The effect of flexibility on the time-averaged flow field is shown in Fig. 24. For the rigid case there is a clear time-averaged jet in the wake of the airfoil implying thrust generation. For the optimal case this time-averaged jet is both broader and slightly stronger implying increased thrust. For the post-optimal case the time-averaged jet is weaker and narrower implying decreased thrust. The underlying reason for this variation in time-averaged jet strength is demonstrated in the phase-averaged vorticity contour plots shown in Fig. 25. The rigid case is shown in the left column, the optimal in the central column, and the post-optimal in the right column. For each case four phases are considered: top, middle (down), bottom, and middle (up). For all three cases the flow fields are qualitatively similar, during the downward motion (Fig. 25a to c) a counter-clockwise TEV forms, and during the upward motion (Fig. 25c to a) its clockwise counterpart forms. These TEVs convect into the wake to form a reverse-Kármán vortex street which is responsible for the time-averaged jets observed in Fig. 24. At the leading-edge a counter-clockwise LEV forms during the upward motion and convects along the lower surface gradually being dissipated such that at the tip of the trailing-edge device it is so weak as to be no longer visible. Its inverse partner is visible above the airfoil in Figures 25b and c.

Quantitatively however the flow fields differ. The TEVs are visibly weaker in the post-optimal case than the optimal, and marginally weaker in the rigid case, this is quantified in Fig. 26. This figure demonstrates that optimal flexibility increases the strength of the TEVs ($\Gamma/U_\infty c$), enhancing the time-averaged jet and thereby increasing drag reduction. This is in agreement with the Kármán and Burgess's equation [23] for thrust due to a reverse-Kármán street. The effect is so strong as to give an almost linear dependency between mean TEV circulation and drag reduction.

IV. Conclusions

Experiments were performed to investigate the effect of amplitude, depth and trailing edge device flexibility on the drag reduction resultant from oscillating a NACA 0012 airfoil at an angle of attack of 0° and Reynolds number of

40,000, across a range of frequencies. At low values of Strouhal number based on amplitude the drag reduction was shown to follow parabolic trends with steeper gradient for greater amplitude in a similar manner to Garrick approximations. At $Sr_A \approx 0.08$ the larger amplitudes break from this trend resulting in a crossover point at $Sr_A \approx 0.12$ after which smaller amplitudes become preferable. The cause was shown to be earlier formation of thrust inhibiting leading edge vortices at larger amplitudes.

Proximity to the surface led to a decrease in drag reduction and a general departure from these trends. In addition drag enhancing peaks were observed for the four smaller amplitudes. These were shown to depend on a critical unsteady parameter of $\tau_c = 0.25$. At this value of τ, large scale free surface waves form that significantly change the flow field in the vicinity of the airfoil inhibiting thrust creation. For depths greater than two chords the free surface has a negligible effect.

Flexibility of the trailing edge device was shown to improve performance resulting in an optimum flexibility. The improvement was shown to be highly amplitude dependent with greater effect for smaller amplitude. The improvement was also shown to be dependent on the length of the device with greater effect for longer length. The peak improvement was therefore 28% for the smallest amplitude and largest device. It was most effective for elastic parameters of $\lambda \approx O(1)$, although a very wide range of elastic parameters were effective. The underlying cause of the improvement was strengthening of the trailing-edge vortices leading to a stronger time-averaged jet.

Acknowledgments

The authors would like to acknowledge the support from the Department of the Navy Grant N62909-10-1-7117 issued by the Office of Naval Research Global.

References

[1]McCormic, M.E., and Bhattach, R., "Drag Reduction of a Submersible Hull by Electrolysis," *Naval Engineers Journal*, Vol. 85, No. 2, 1973, pp. 11-16.

[2]Shen, X.C., Ceccio, S.L., and Perlin, M., "Influence of Bubble Size on Micro-Bubble Drag Reduction," *Experiments in Fluids*, Vol. 41, No. 3, 2006, pp. 415-424.

[3]Winkel, E.S., Oweis, G.F., Vanapalli, S.A., Dowling, D.R., Perlin, M., Solomon, M.J., et al., "High-Reynolds-Number Turbulent Boundary Layer Friction Drag Reduction from Wall-Injected Polymer Solutions," *Journal of Fluid Mechanics*, Vol. 621, 2009, pp. 259-288.

[4]Cleaver, D.J., Wang, Z., and Gursul, I. "Vortex Mode Bifurcation and Lift Force of a Plunging Airfoil at Low Reynolds Numbers," 48th AIAA Aerospace Sciences Meeting, AIAA 2010-390, 2010.

[5]Tuncer, I.H., and Kaya, M., "Optimization of Flapping Airfoils for Maximum Thrust and Propulsive Efficiency," *AIAA Journal*, Vol. 43, No. 11, 2005, pp. 2329-2336.

[6]Young, J., and Lai, J.C.S., "Oscillation Frequency and Amplitude Effects on the Wake of a Plunging Airfoil," *AIAA Journal*, Vol. 42, No. 10, 2004, pp. 2042-2052.

[7]Jones, K.D., Dohring, C.M., and Platzer, M.F., "Experimental and Computational Investigation of the Knoller-Betz Effect," *AIAA Journal*, Vol. 36, No. 7, 1998, pp. 1240-1246.

[8]Cleaver, D.J., Wang, Z., and Gursul, I., "Lift Enhancement by Means of Small Amplitude Airfoil Oscillations at Low Reynolds Numbers," *AIAA Journal*, Vol. 49, No. 9, 2011, pp. 2018 - 2033.

[9]Naito, S., and Isshiki, H., "Effect of Bow Wings on Ship Propulsion and Motions," *Applied Mechanics Reviews*, Vol. 58, No. 4, 2005, pp. 253-268.

[10]Michell, J.H., "The Highest Waves in Water," *Philosophical Magazine Series 5*, Vol. 36, 1893, pp. 430-437.

[11]Tsuji, Y., and Nagata, Y., "Stokes' Expansion of Internal Deep Water Waves to the Fifth Order," *Journal of Oceanography*, Vol. 29, No. 2, 1973, pp. 61-69.

[12]Heathcote, S., and Gursul, I., "Flexible Flapping Airfoil Propulsion at Low Reynolds Numbers," *AIAA Journal*, Vol. 45, No. 5, 2007, pp. 1066-1079.

[13]Moffat, R.J., "Using Uncertainty Analysis in the Planning of an Experiment," *Journal of Fluids Engineering - Transactions of the ASME*, Vol. 107, No. 2, 1985, pp. 173-178.

[14]Heathcote, S. "Flexible Flapping Airfoil Propulsion at Low Reynolds Numbers," *Ph.D. Dissertation*, Dept of Mechanical Engineering, University of Bath, Bath, 2006.

[15]Frampton, K.D., Goldfarb, M., Monopoli, D., and Cveticanin, D. "Passive Aeroelastic Tailoring for Optimal Flapping Wings," Proceedings of Conference on Fixed, Flapping and Rotary Wing Vehicles at Very Low Reynolds Numbers, 2000, pp. 473-482.
[16]Heathcote, S., Wang, Z., and Gursul, I., "Effect of Spanwise Flexibility on Flapping Wing Propulsion," *Journal of Fluids and Structures*, Vol. 24, No. 2, 2008, pp. 183-199.
[17]Calderon, D.E., Wang, Z., and Gursul, I. "Lift Enhancement of a Rectangular Wing Undergoing a Small Amplitude Plunging Motion," 48th AIAA Aerospace Sciences Meeting Including the New Horizons Forum and Aerospace Exposition, AIAA 2010-386, 2010.
[18]Cleaver, D.J., Wang, Z.J., and Gursul, I. "Delay of Stall by Small Amplitude Airfoil Oscillation at Low Reynolds Numbers," 47th AIAA Aerospace Sciences Meeting, AIAA Paper 2009-392, 2009.
[19]Cleaver, D.J., Wang, Z.J., and Gursul, I. "Lift Enhancement on Oscillating Airfoils," 39th AIAA Fluid Dynamics Conference, AIAA Paper 2009-4028, 2009.
[20]Young, J., and Lai, J.C.S., "Vortex Lock-in Phenomenon in the Wake of a Plunging Airfoil," *AIAA Journal*, Vol. 45, No. 2, 2007, pp. 485-490.
[21]Huang, R.F., and Lee, H.W., "Turbulence Effect on Frequency Characteristics of Unsteady Motions in Wake of Wing," *AIAA Journal*, Vol. 38, No. 1, 2000, pp. 87-94.
[22]Visbal, M.R., "High-Fidelity Simulation of Transitional Flows Past a Plunging Airfoil," *AIAA Journal*, Vol. 47, No. 11, 2009, pp. 2685-2697.
[23]Streitlien, K., and Triantafyllou, G.S., "On Thrust Estimates for Flapping Foils," *Journal of Fluids and Structures*, Vol. 12, No. 1, 1998, pp. 47-55.
[24]Tuncer, I.H., Walz, R., and Platzer, M.F. "A Computational Study on the Dynamic Stall of a Flapping Airfoil," 16th AIAA Applied Aerodynamics Conference, AIAA Paper 98-2519, 1998.
[25]Zhu, Q., Liu, Y., and Yue, D., "Dynamics of a Three-Dimensional Oscillating Foil near the Free Surface," *AIAA Journal*, Vol. 44, No. 12, 2006, pp. 2997-3009.

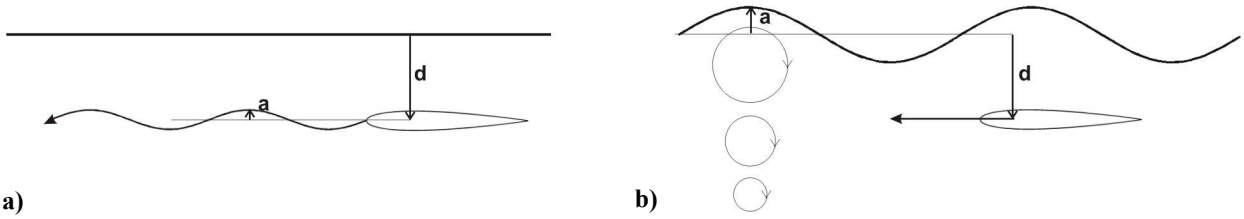

Fig. 1 Scenarios for hydrofoil unsteadiness: a) forced motion in calm water, b) passive motion due to wave unsteadiness.

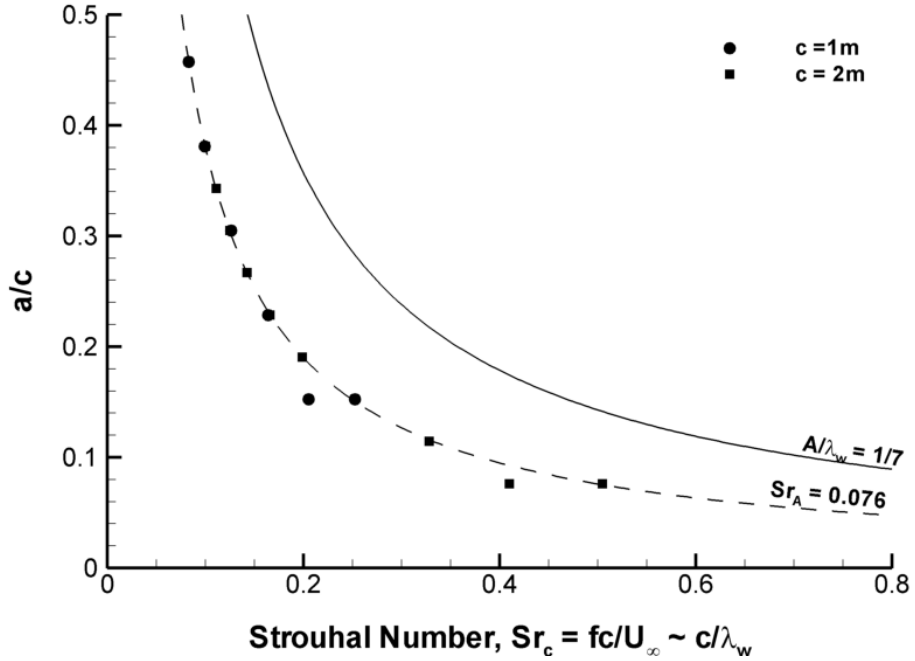

Fig. 2 Range of experimental parameters. Symbols represent values from sea state tables assuming a chord length of c = 1 m or 2 m, dashed line represents constant Sr_A = 0.076, and solid line represents constant A/λ_w = 1/7 (Sr_A = 0.142) as predicted for a Stokes ideal wave.

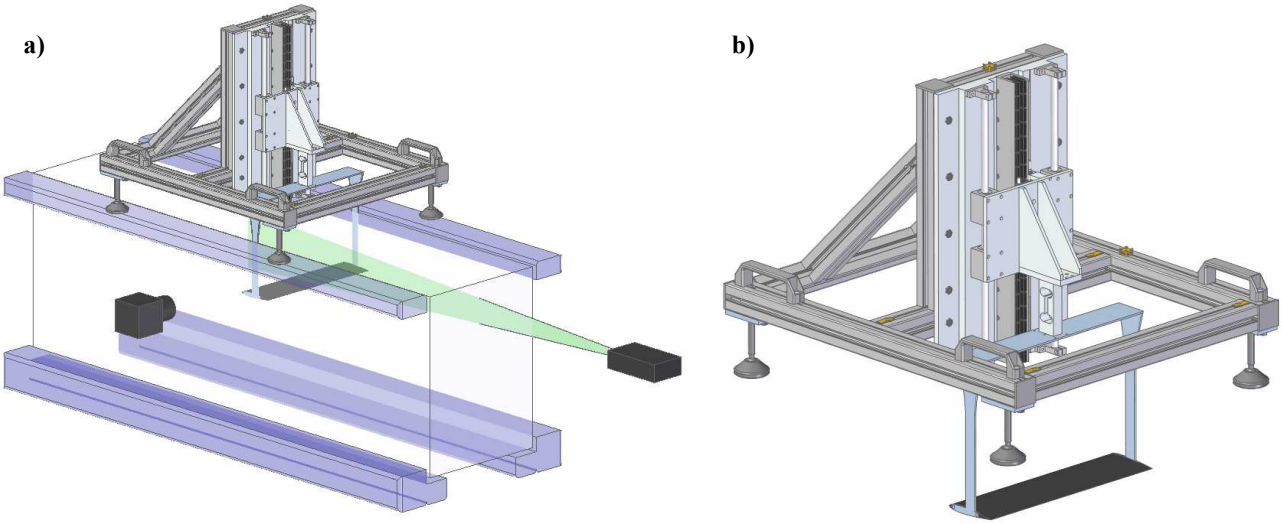

Fig. 3 a) Test section with PIV equipment, and b) experimental rig.

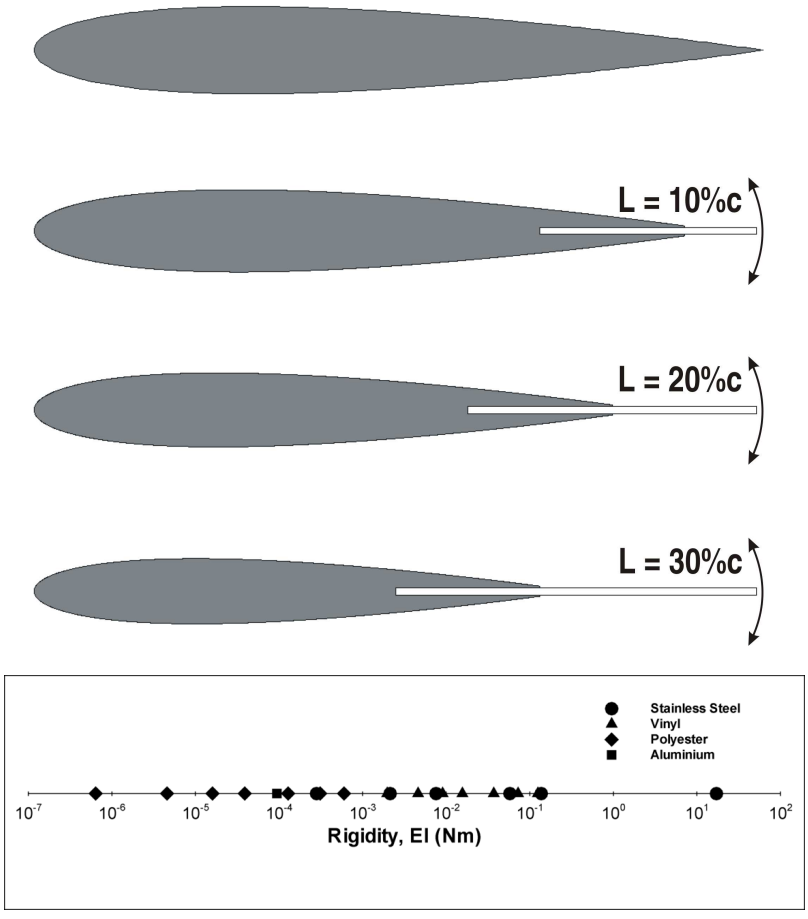

Fig. 4 Cross section of wing profiles, in descending order: NACA 0012, 10%c, 20%c, and 30%c flexible trailing edge device. The thickness of the trailing edge device shown is the maximum of 1mm. Inset shows the range of possible rigidities achieved through the use of 21 combinations of material and thickness.

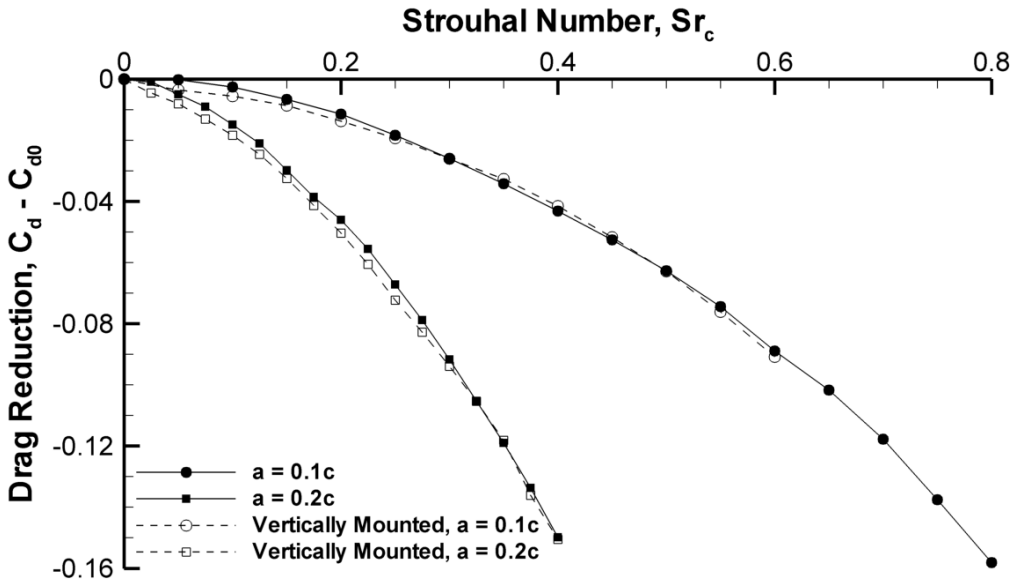

Fig. 5 Comparison of results obtained with the current experimental setup and the vertical rig as previously used in Heathcote et al.[16], Calderon et al. [17], and Cleaver et al. [4,8,18,19].

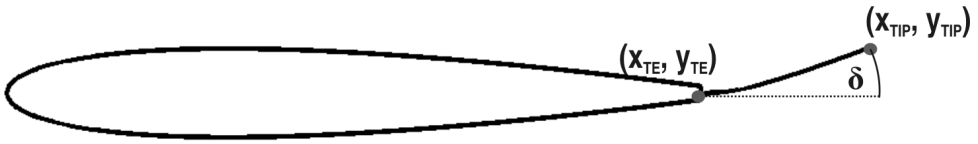

a)

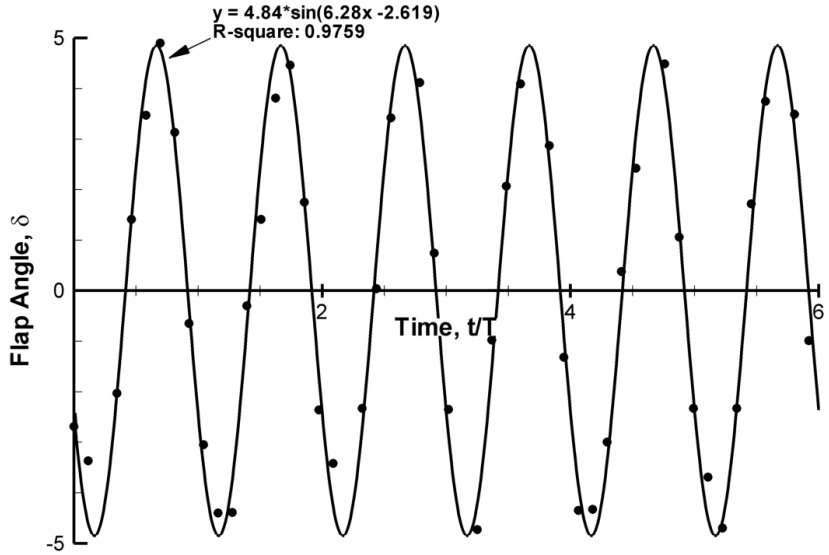

b)

Fig. 6 Deformation measurements: a) coordinates used for motion tracking, b) typical sinusoidal curve fit. Symbols denote experimental data derived from the PIV images; line represents the sinusoidal curve fit. Case shown is L_{TED} = 0.2*c*, *s* = 0.076 mm, *a/c* = 0.1, and Sr_A = 0.08.

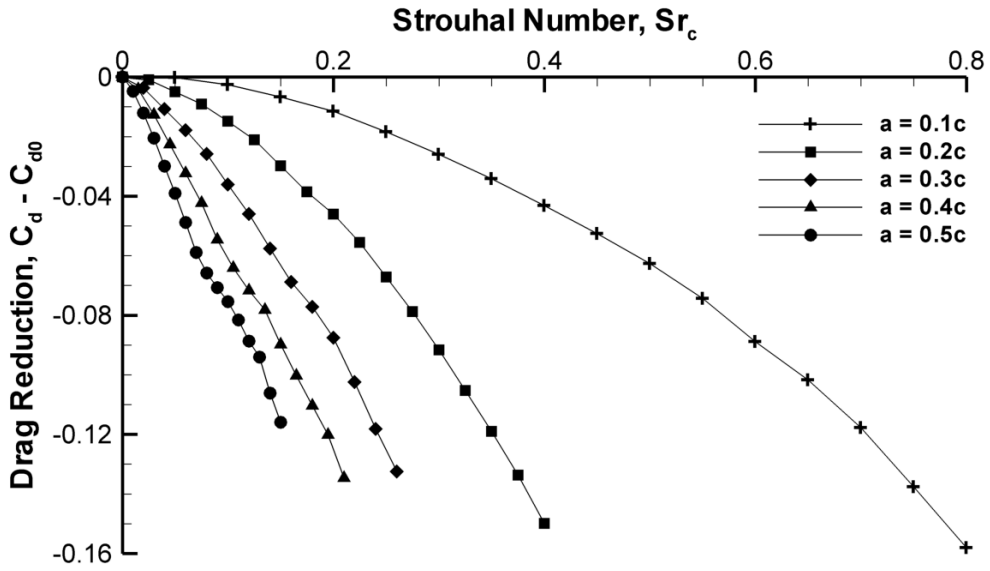

Fig. 7 Time-averaged reduction in drag coefficient against Strouhal number based on chord for a NACA 0012 airfoil oscillated at the central depth (*d/c* = 2.25).

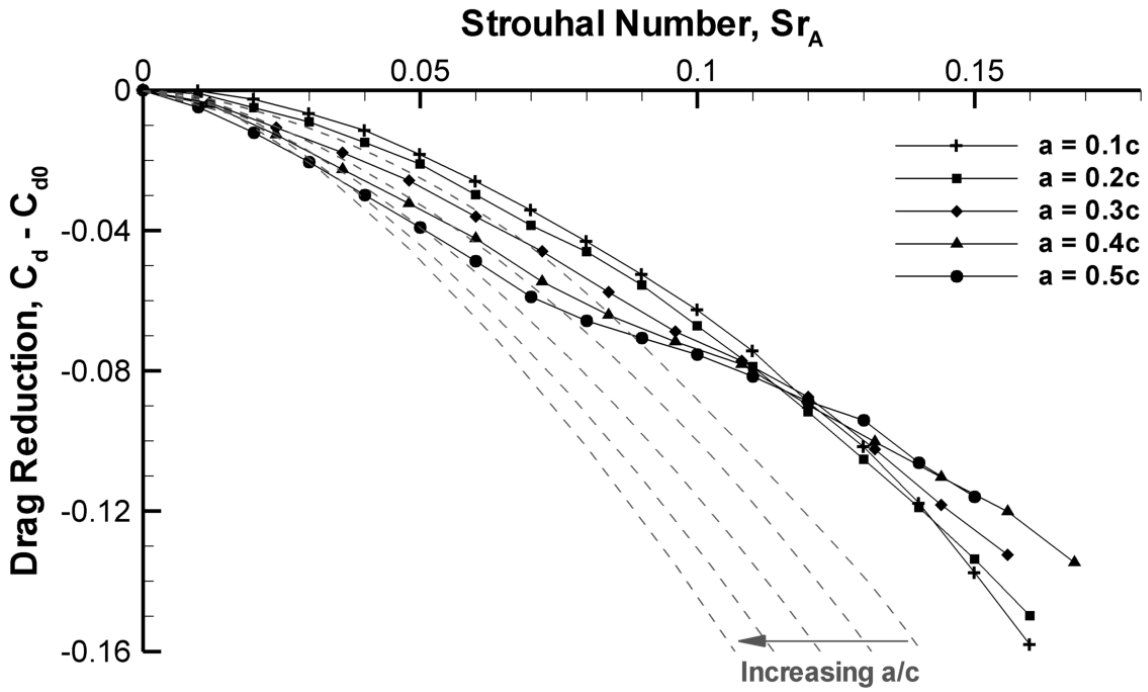

Fig. 8 Time-averaged reduction in drag coefficient against Strouhal number based on amplitude for a NACA 0012 airfoil oscillated at the central depth (*d/c* = 2.25). Dashed lines represent Garrick approximations for the same amplitudes.

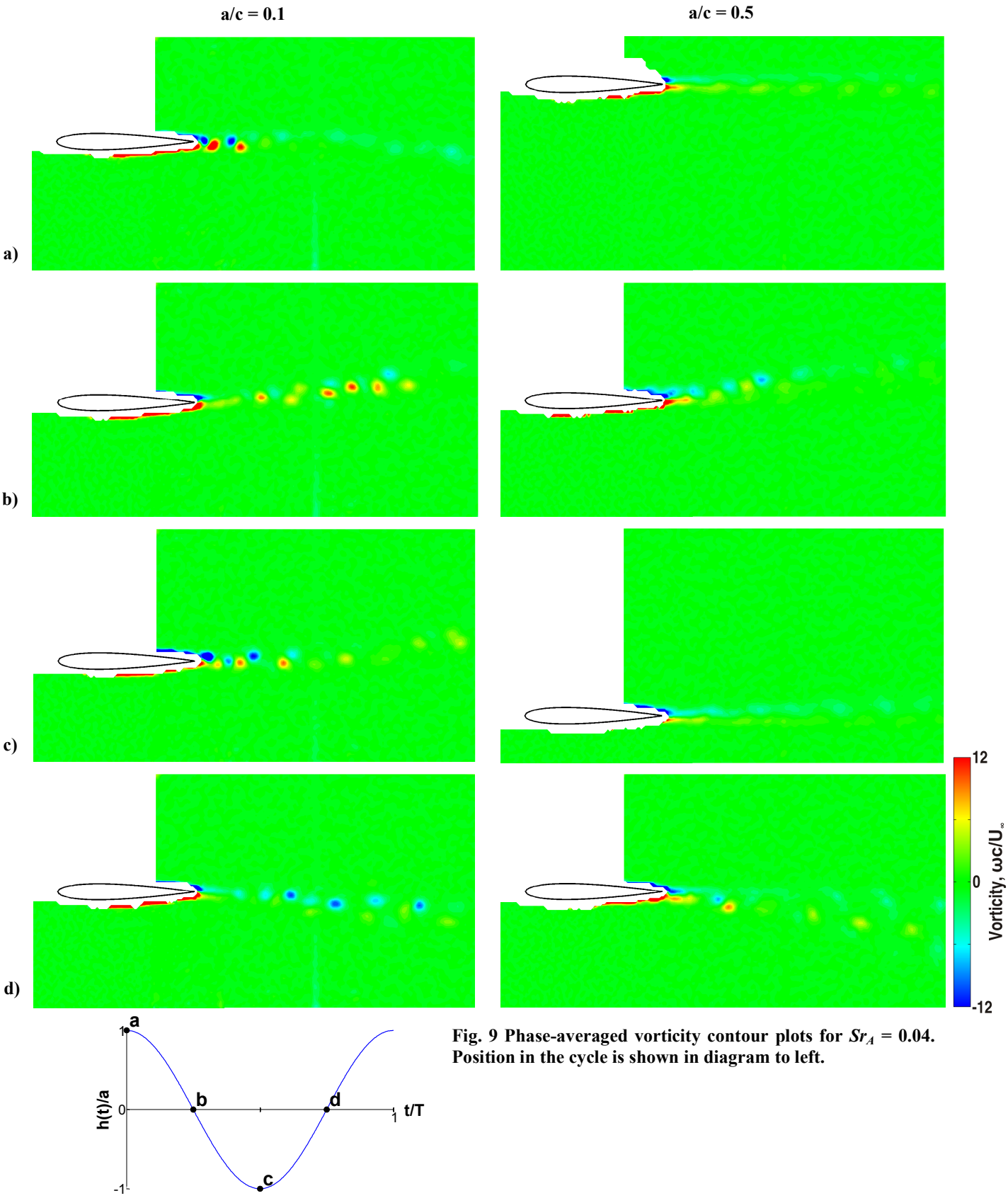

Fig. 9 Phase-averaged vorticity contour plots for Sr_A = 0.04. Position in the cycle is shown in diagram to left.

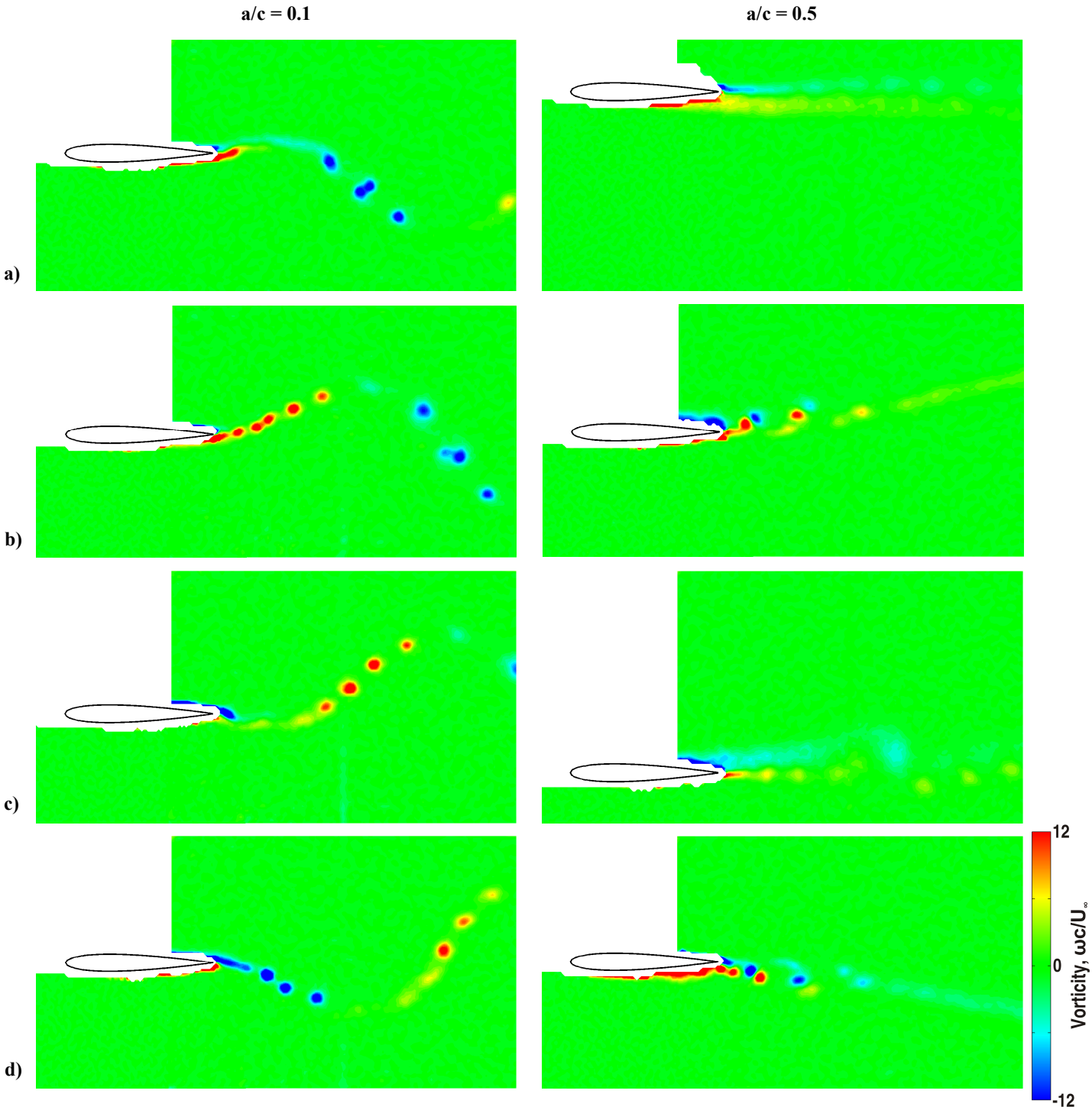

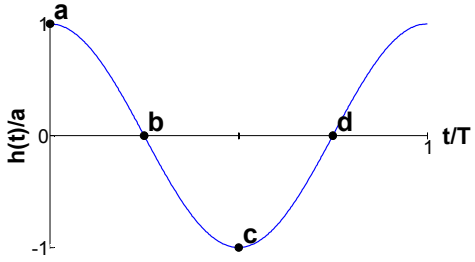

Fig. 10 Phase-averaged vorticity contour plots for Sr_A = 0.08. Position in the cycle is shown in diagram to left.

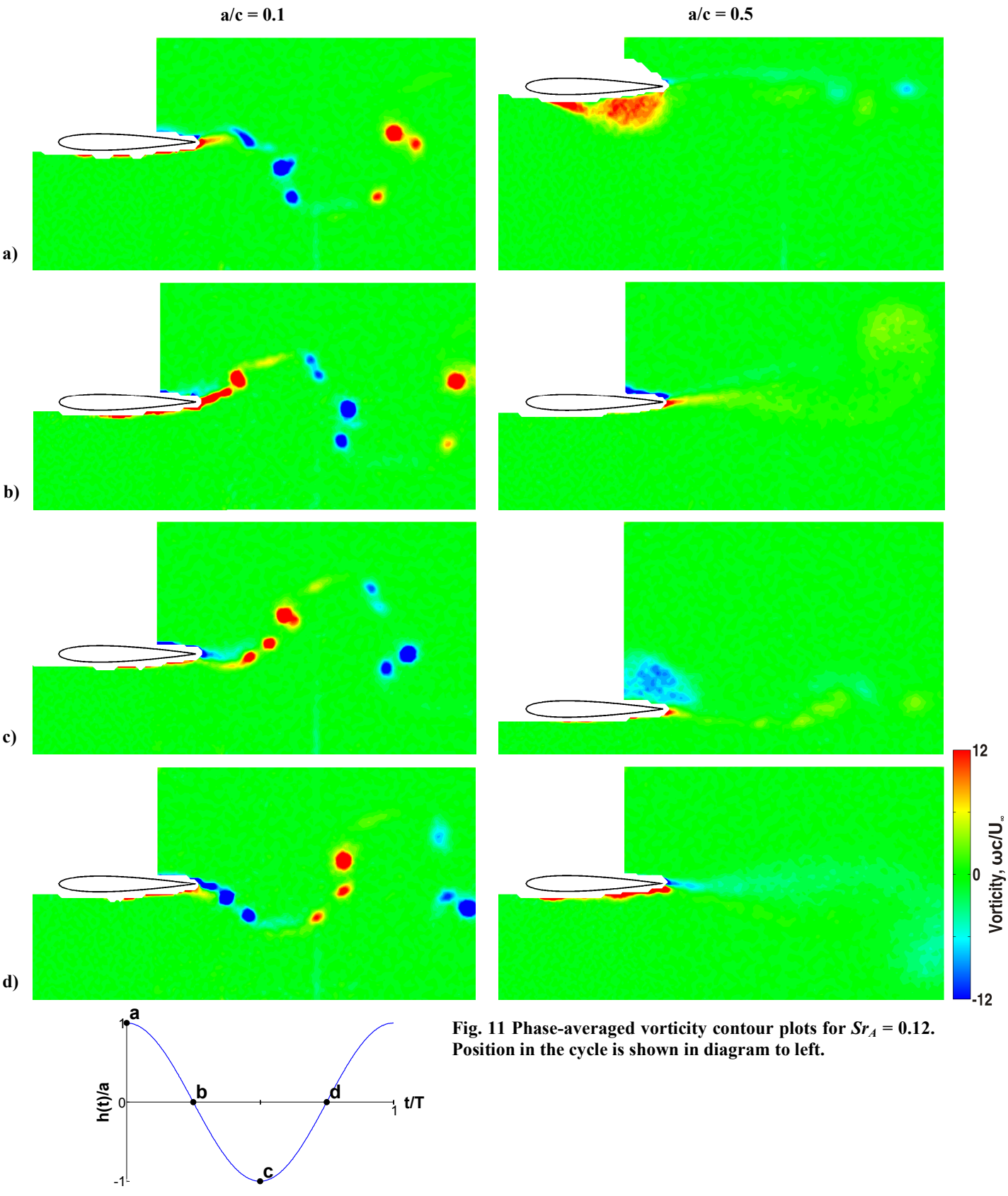

Fig. 11 Phase-averaged vorticity contour plots for Sr_A = 0.12. Position in the cycle is shown in diagram to left.

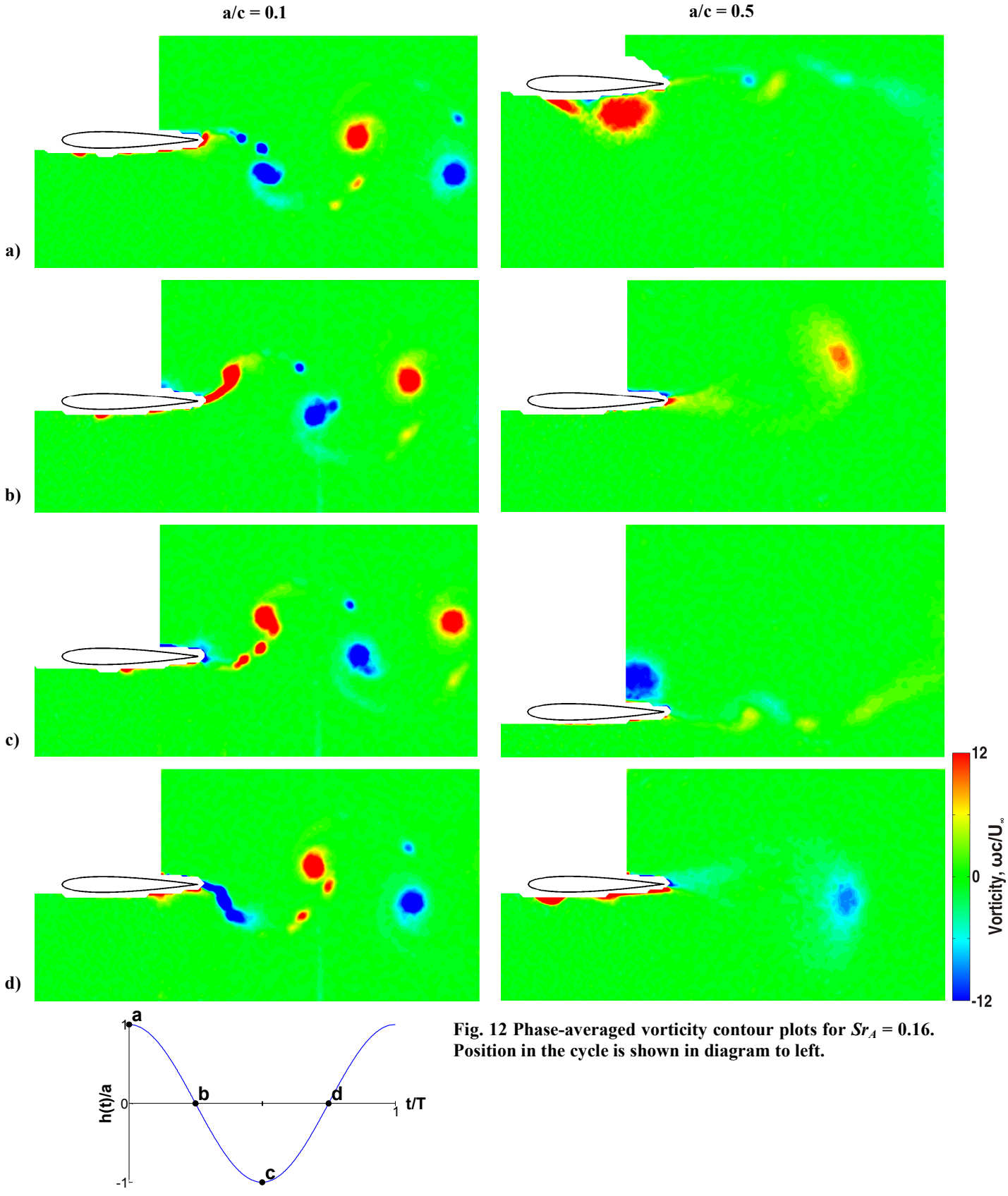

Fig. 12 Phase-averaged vorticity contour plots for Sr_A = 0.16. Position in the cycle is shown in diagram to left.

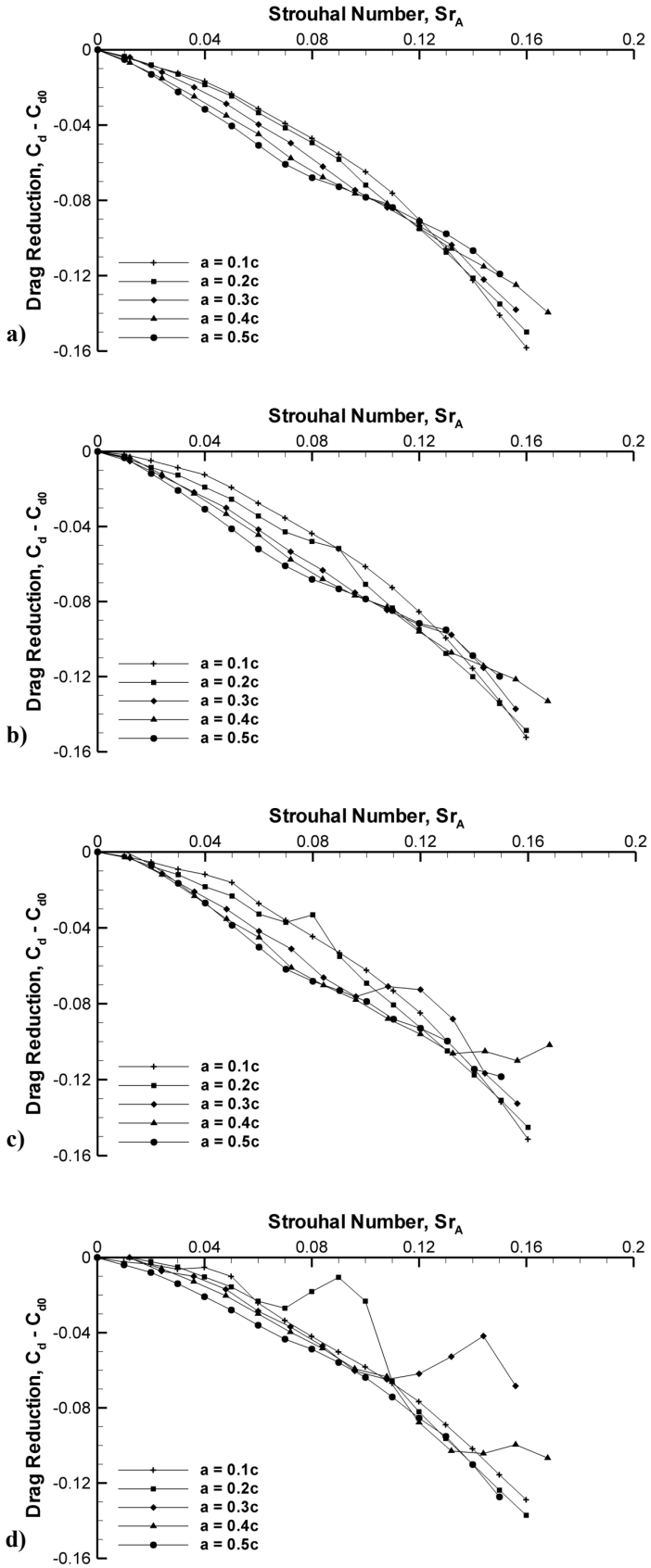

Fig. 13 Time-averaged reduction in drag coefficient against Strouhal number based on amplitude for a NACA 0012 airfoil oscillated at depths of: a) *d/c* = 2.0, b) *d/c* = 1.5, c) *d/c* = 1.0, and d) *d/c* = 0.5.

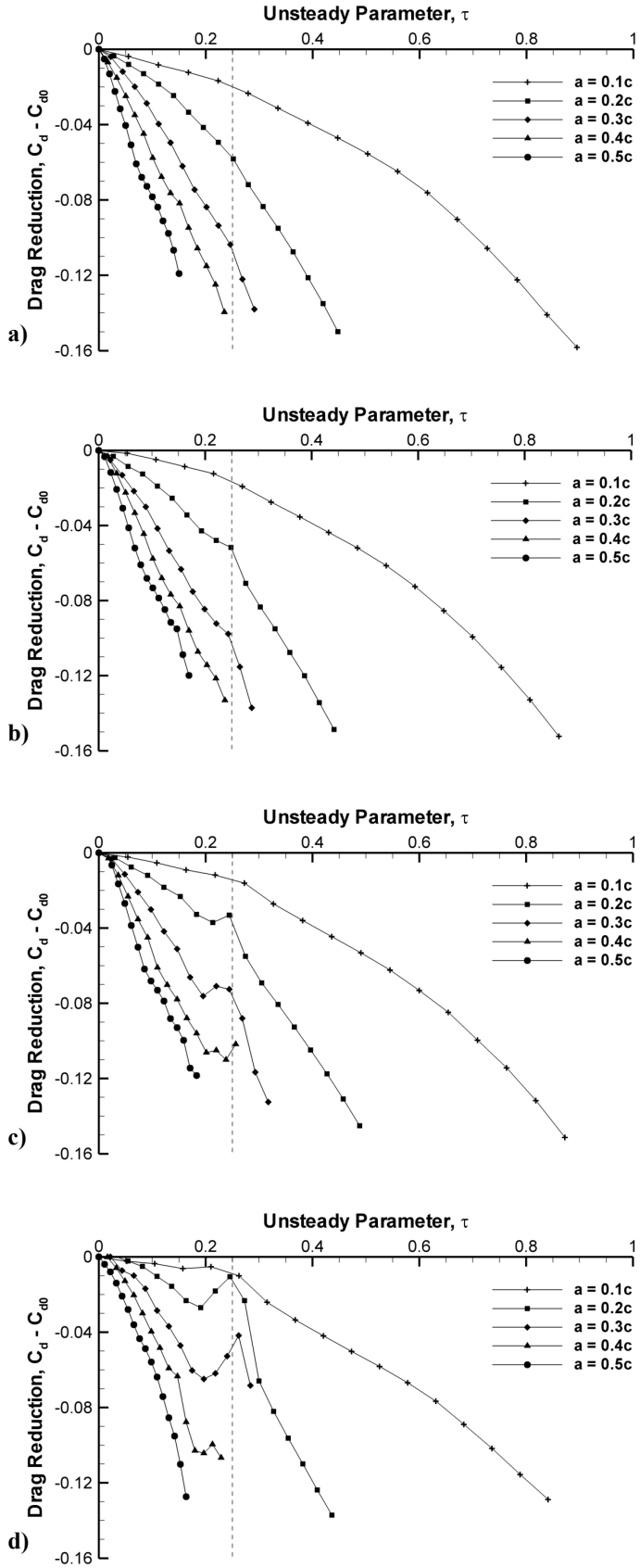

Fig. 14 Time-averaged reduction in drag coefficient against unsteady parameter for a NACA 0012 airfoil oscillated at depths of: a) *d/c* = 2.0, b) *d/c* = 1.5, c) *d/c* = 1.0, and d) *d/c* = 0.5.

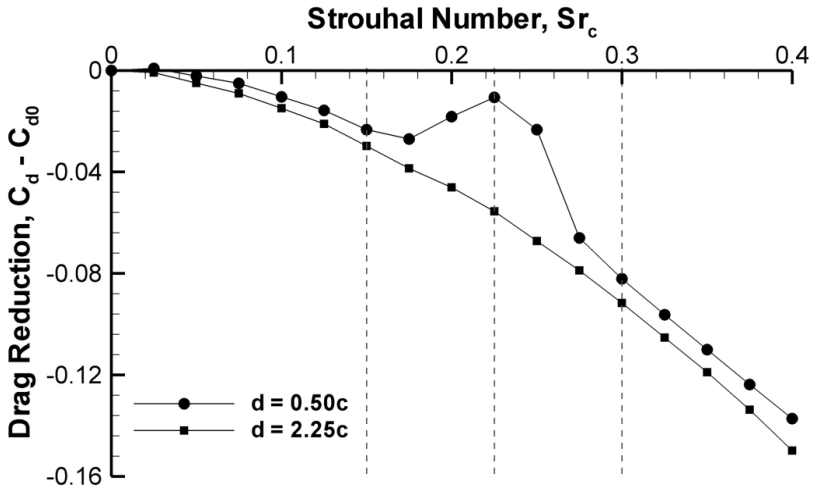

Fig. 15 Time-averaged reduction in drag coefficient against Strouhal number based on chord, for a NACA 0012 airfoil oscillated at *a/c* = 0.2 at depths of *d/c* = 2.25 and *d/c* = 0.5. Dashed lines denote the Strouhal numbers used in Figures 16 through 18.

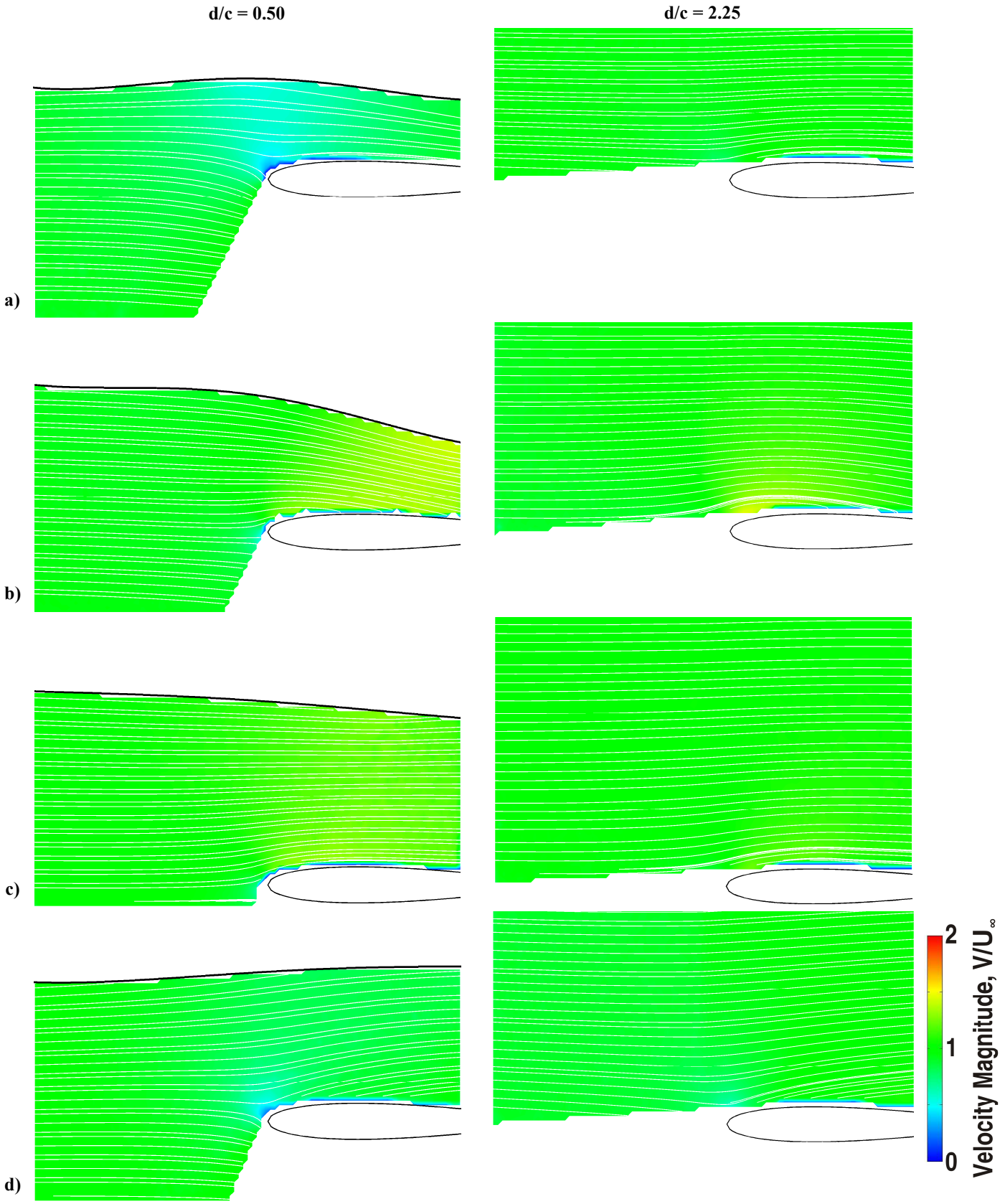

Fig. 16 Phase-averaged velocity magnitude contour plots for *a/c* = 0.20, and Sr_c = 0.150. Left column is *d/c* = 0.50 and right column is *d/c* = 2.25. a) top, b) middle (down), c) bottom and d) middle (up) of the motion.

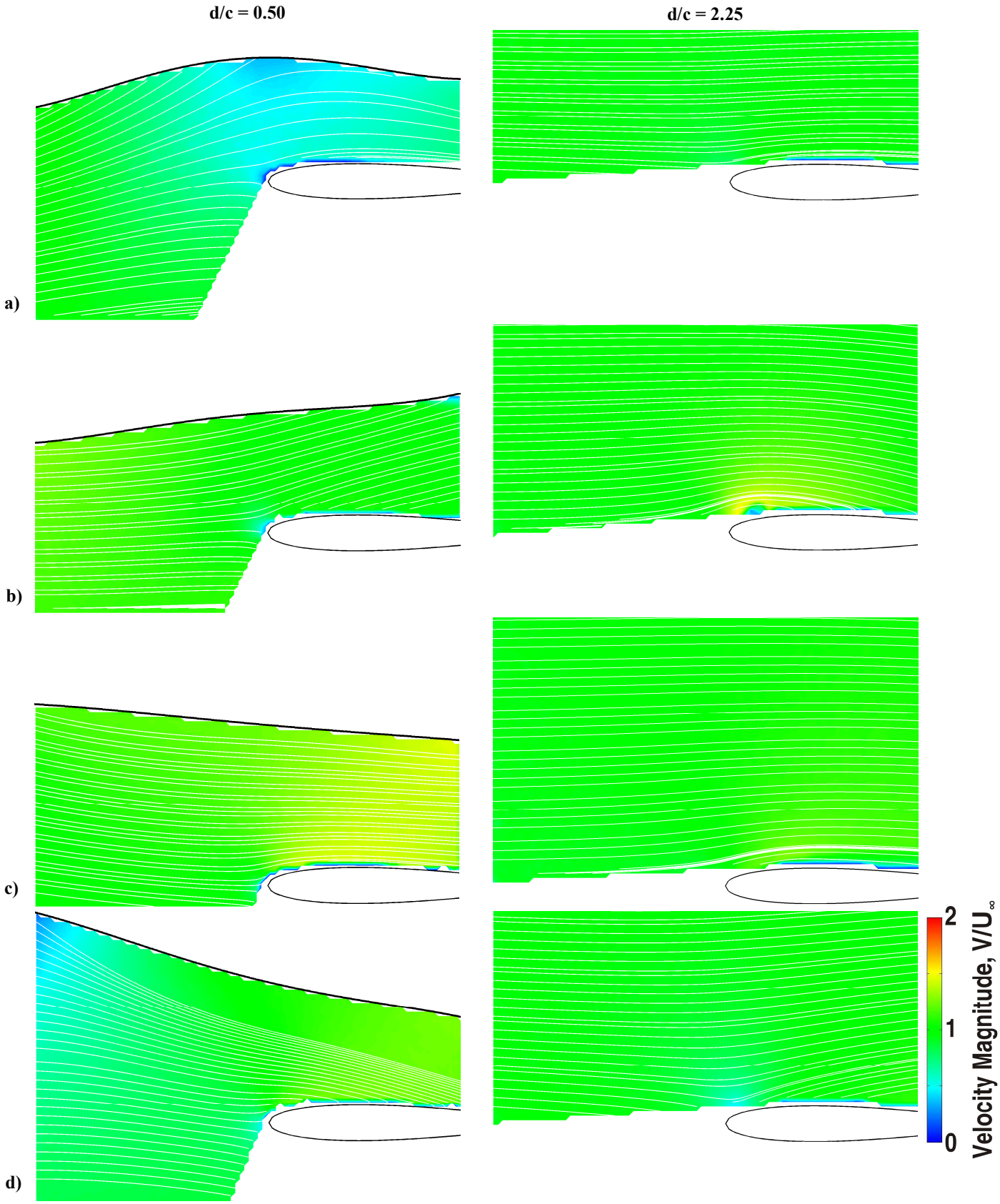

Fig. 17 Phase-averaged velocity magnitude contour plots for *a/c* = 0.20, and Sr_c = 0.225. Left column is *d/c* = 0.50 and right column is *d/c* = 2.25. a) top, b) middle (down), c) bottom and d) middle (up) of the motion.

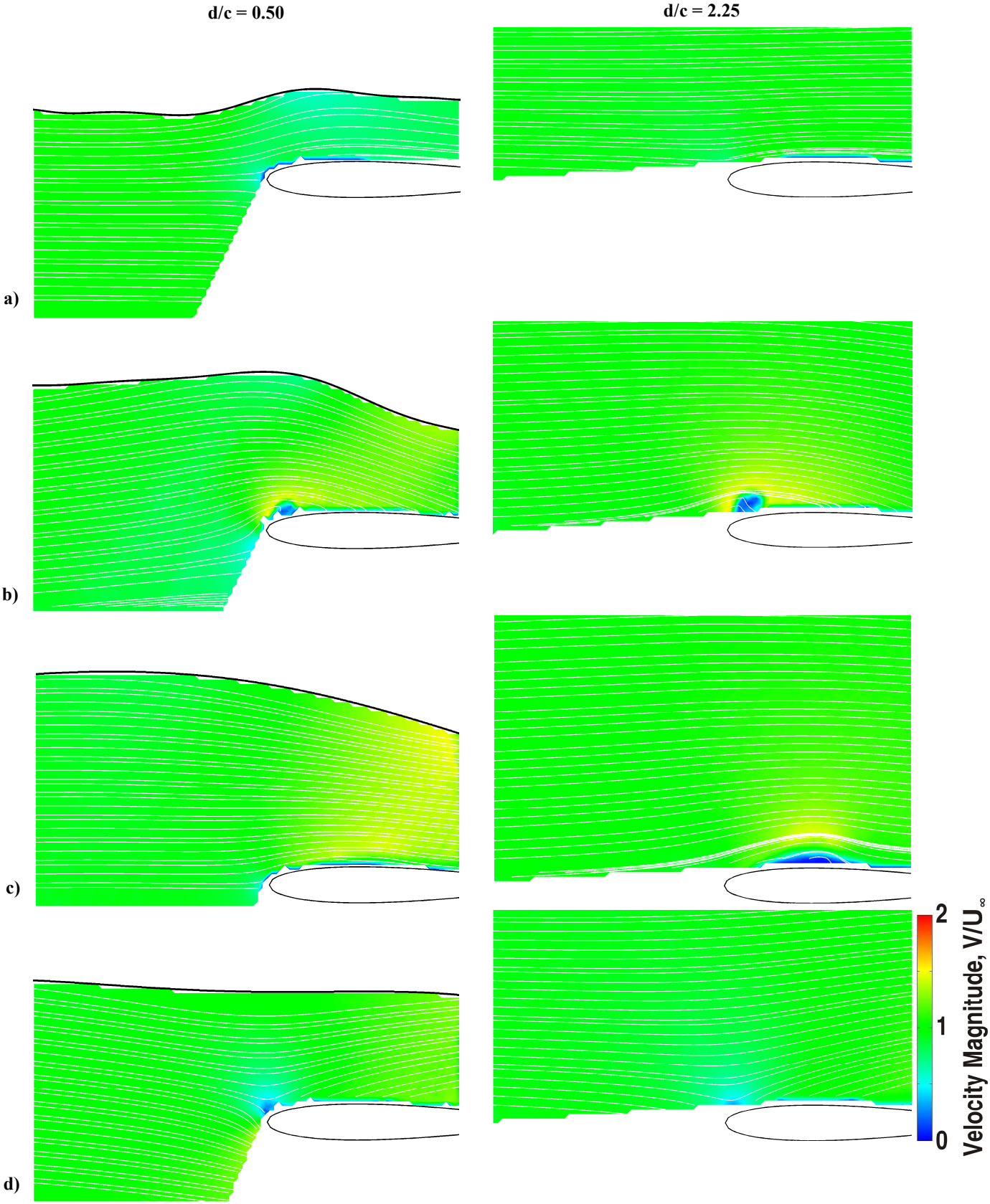

Fig. 18 Phase-averaged velocity magnitude contour plots for *a/c* = 0.20, and Sr_c = 0.300. Left column is *d/c* = 0.50 and right column is *d/c* = 2.25. a) top, b) middle (down), c) bottom and d) middle (up) of the motion.

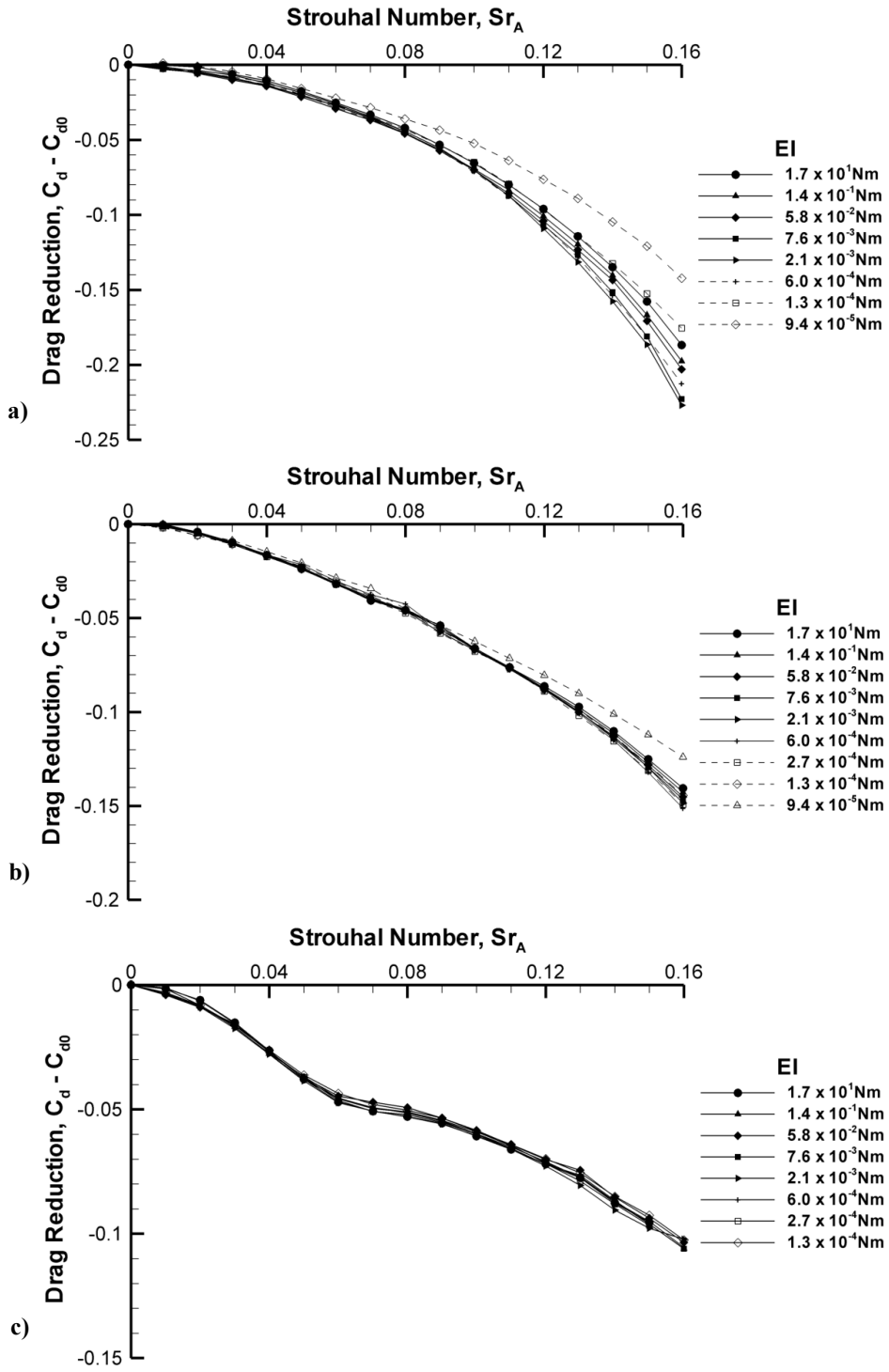

Fig. 19 Time-averaged reduction in drag coefficient against Strouhal number based on amplitude for an airfoil with flexible trailing edge device (rigidity shown in legend) of length L_{TED} = 0.2*c* oscillated at *d/c* = 2.25 and amplitudes of: a) *a/c* = 0.1, b) *a/c* = 0.2, and c) *a/c* = 0.5.

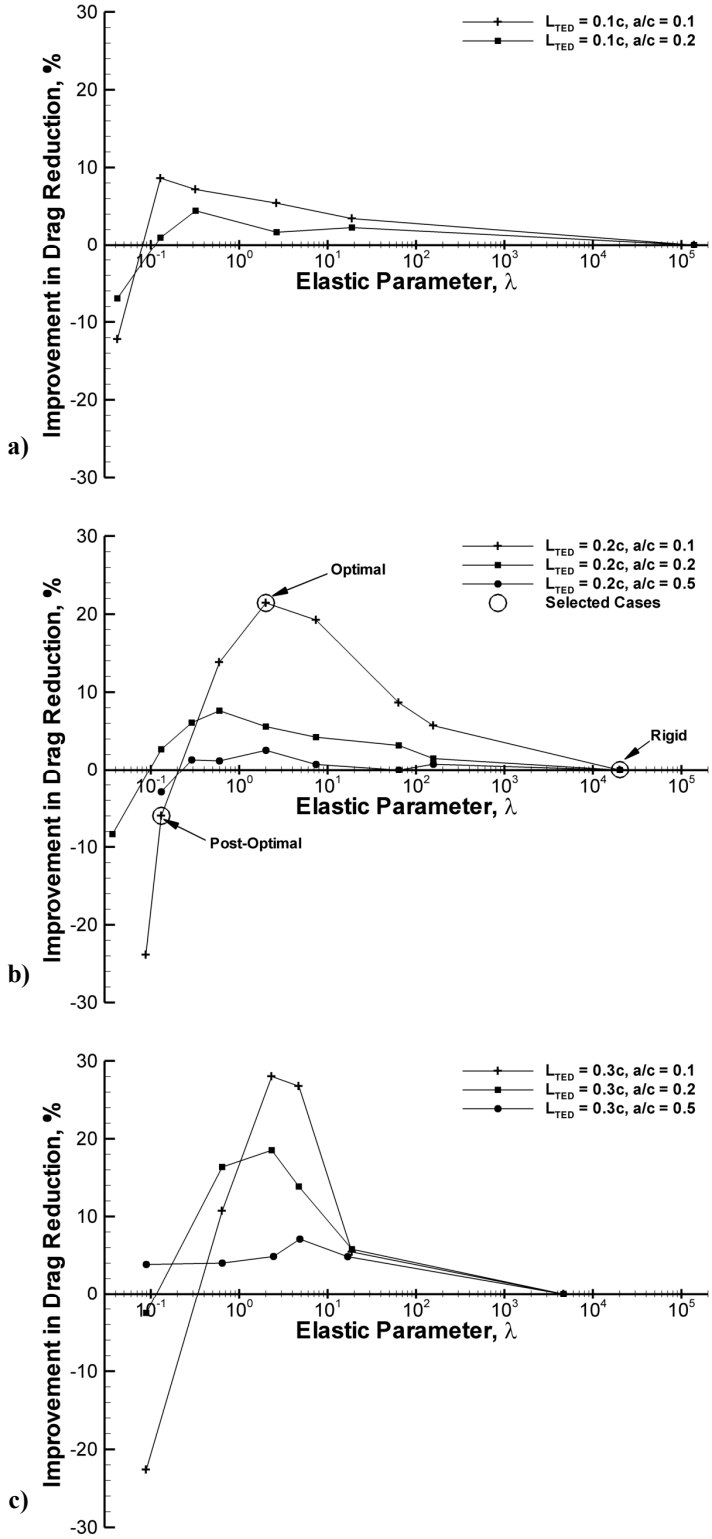

Fig. 20 Improvement in drag reduction due to flexibility at the maximum Strouhal number tested for: a) L_{TED} = 0.1*c*, b) L_{TED} = 0.2*c*, and c) L_{TED} = 0.3*c*. Highlighted rigid, optimal, and pot-optimal points in b) are used in Figures 22 to 26.

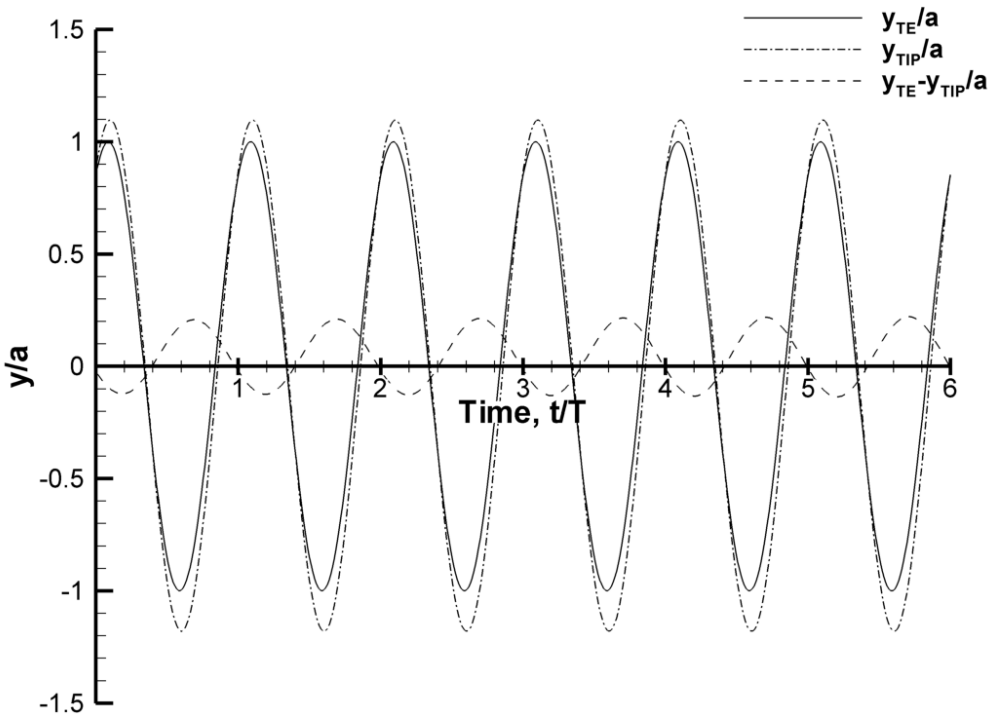

Fig. 21 Example motion tracking curves. Note the phase lead of the deformation (dashed line).

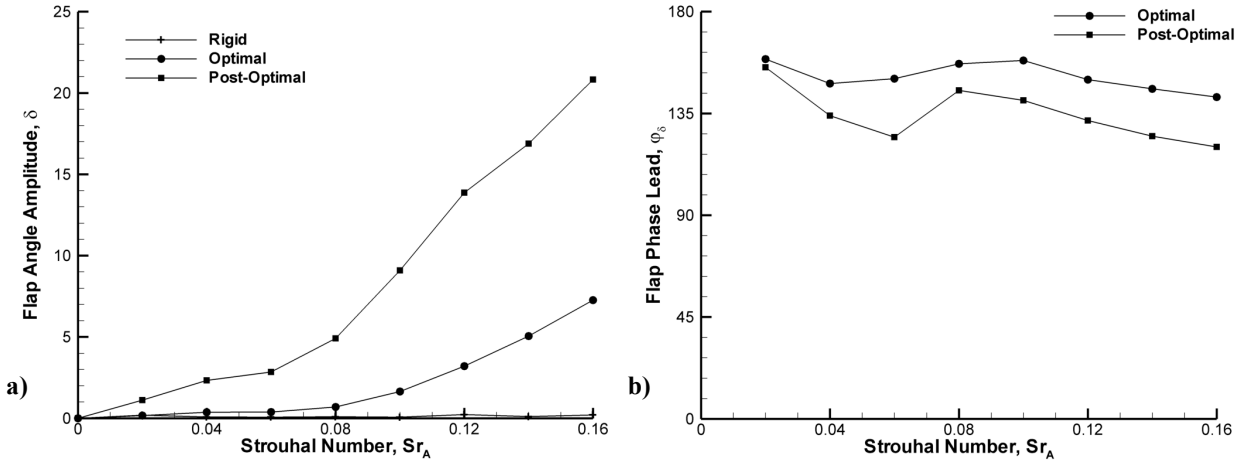

Fig. 22 a) flap angle amplitude, and b) flap phase lead for L_{TED} = 0.2*c*, and *a/c* = 0.1. It was not possible to measure the phase lead for the rigid case due to the flap angle being approximately zero.

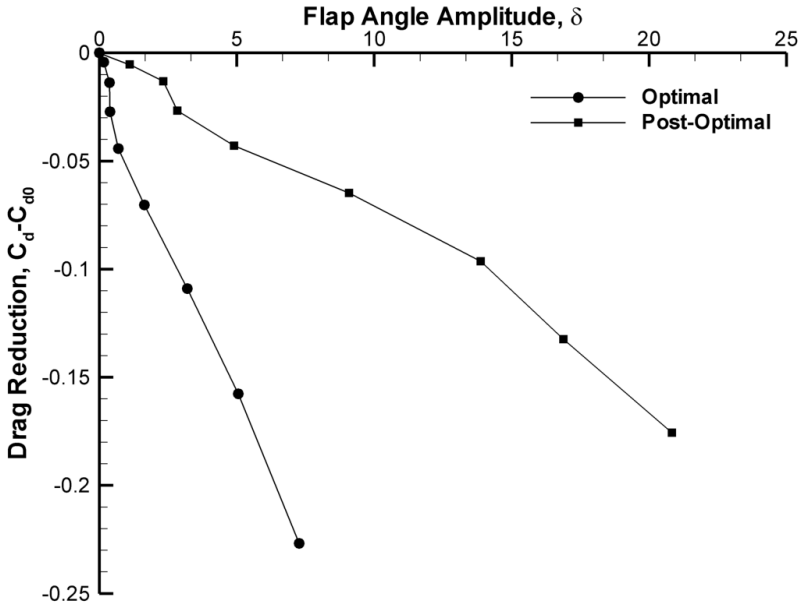

Fig. 23 Flap angle amplitude versus drag reduction for L_{TED} = 0.2*c*, and *a/c* = 0.1.

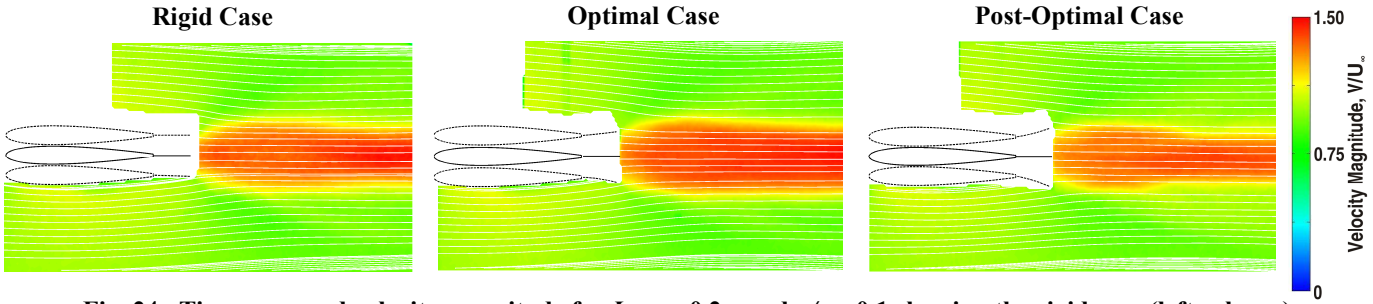

Fig. 24 Time-averaged velocity magnitude for L_{TED} = 0.2c, and a/c = 0.1 showing the rigid case (left column), optimal case (central column) and post-optimal case (right column) across a range of Strouhal numbers.

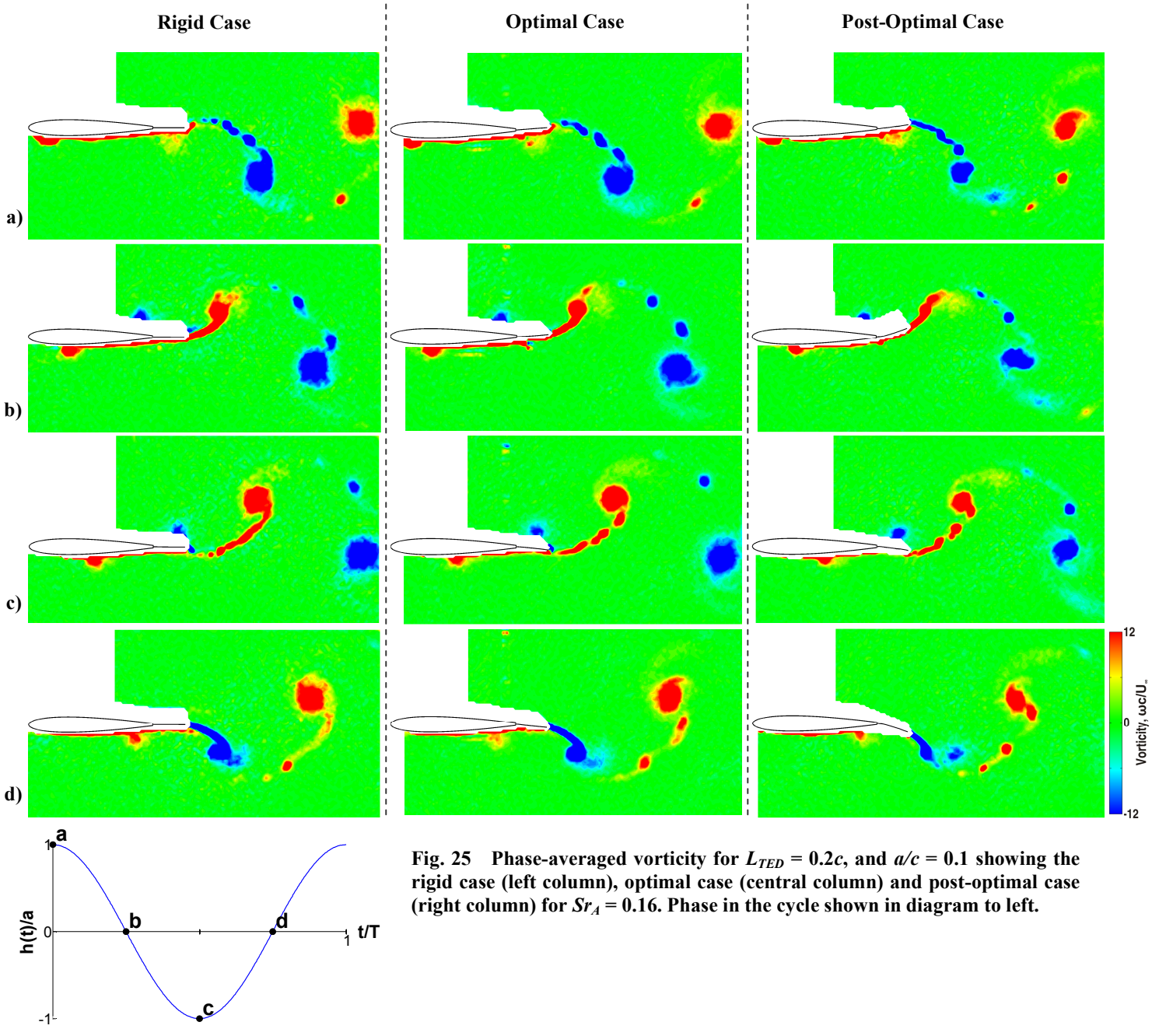

Fig. 25 Phase-averaged vorticity for L_{TED} = 0.2c, and a/c = 0.1 showing the rigid case (left column), optimal case (central column) and post-optimal case (right column) for Sr_A = 0.16. Phase in the cycle shown in diagram to left.

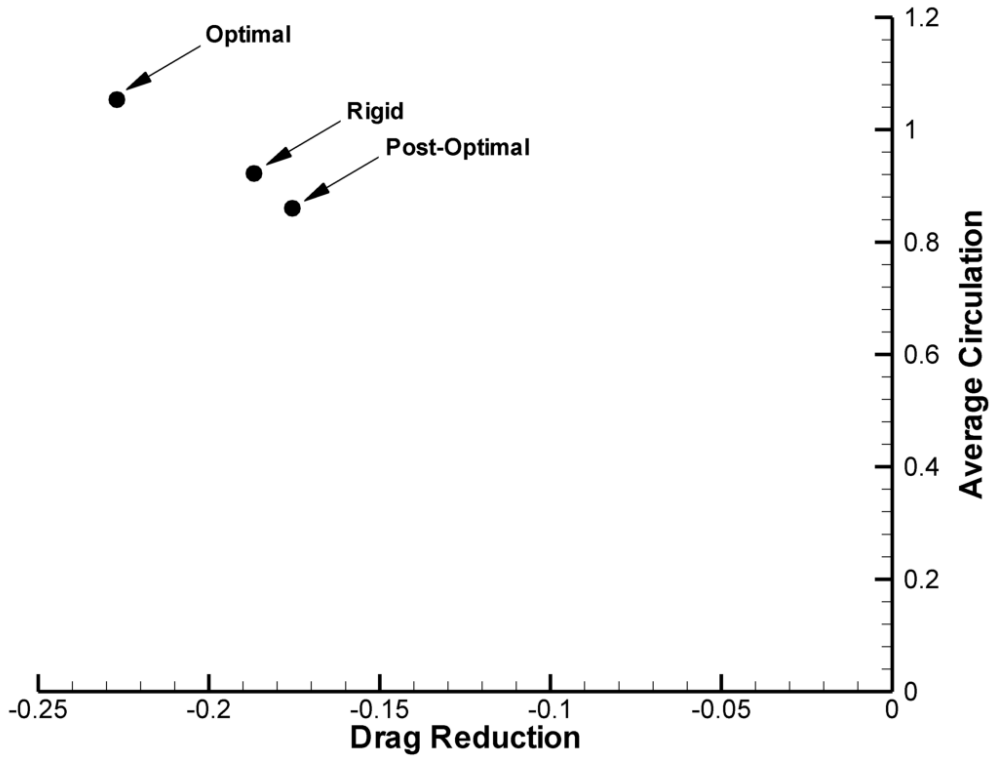

Fig. 26 Average normalized circulation of clockwise and counter-clockwise trailing-edge vortices versus drag reduction.